이학석사 학위논문

Light Curve and Color Properties of Type Ib/Ic Supernovae

Ib/Ic형 초신성의 광도 곡선과 색지수 특성 연구

2021년 2월

서울대학교 대학원

물리·천문학부 천문학전공

진 하 림

Light Curve and Color Properties of Type Ib/Ic Supernovae

by

Harim Jin

A dissertation submitted in partial fulfillment of the requirements for the degree of

Master of Science

in

Astronomy

in

Astronomy Program
Department of Physics and Astronomy
Seoul National University

Committee:

Professor Bon-Chul Koo

Professor Sung-Chul Yoon

Professor Myungshin Im

Light Curve and Color Properties of Type Ib/Ic Supernovae

Ib/Ic형 초신성의 광도 곡선과 색지수 특성 연구

지도교수 윤 성 철

이 논문을 이학석사 학위논문으로 제출함

2020년 10월

서울대학교 대학원

물리·천문학부 천문학전공

진 하 림

진 하 림의 이학석사 학위논문을 인준함

2020년 12월

위 원 장 _____

부 위 원 장 _____

위 원 _____

ABSTRACT

Discussions on supernovae (SNe) progenitors have been conducted from various viewpoints: stellar evolutionary, observational, cosmological, etc. Except for a few cases, direct observations of progenitors are not available, but we can infer their properties from observational data after the explosions. The light curves and color of SNe are important photometric data in determining the chemical compositions of the progenitors and the hydrodynamic properties of SNe. By investigating the light curves and color of SNe, this thesis explores circumstellar matter (CSM) around the progenitors of some peculiar Type Ic SNe and the difference between the progenitors of Type Ib and Type Ic SNe through their color difference. The research was conducted by constructing SN models using the radiation hydrodynamics code STELLA and by comparing the observations and the models.

The first study focuses on the unusual SNe Ic that emits bright optical emission due to shock cooling emission. Since progenitors of SNe Ic are compact stars of which their hydrogen and helium envelopes are stripped off, they experience a significant adiabatic cooling after the explosion. Thus in the early days when the heat from ^{56}Ni radioactive decay has not yet reached the photosphere, the optical brightness is generally faint. However, three SNe Ic observed so far (LSQ14efd, iPTF15dtg, SN 2020bvc) show bright optical light curves during early times. This phenomenon can be explained by the interaction with CSM formed by progenitors before the explosions. Through the simulations, the effects of CSM parameters and explosion parameters on the early time light curve brightness, duration, and color evolution are investigated. The best-fit models are determined for each SN by comparing the light curves and color evolution of the models with the observations. The progenitors of the three unusual SNe Ic are expected to have had massive CSM, the mass of which corresponds to about $0.1 M_{\odot}$. The corresponding mass-loss rate is $\dot{M} \gtrsim 1.0\ M_{\odot}\ \mathrm{yr}^{-1}$

within about one year before the SN explosion, which cannot be explained by the conventional stellar wind or eruptions, requiring a new mass-loss mechanism.

In the second study, photometric data of SNe Ib/Ic are compiled from the literature, and their distributions of $B-V$ color at the V-band peak are compared. We find that SNe Ib are systematically bluer than SNe Ic. To explain this, three possibilities are examined: the difference in the chemical structures of SNe Ib and Ic progenitors, the different degrees of ^{56}Ni mixing, and the different ratio of the ^{56}Ni mass to the ejecta mass. Based on the progenitors with and without helium envelopes, SN models are constructed with various ejecta masses, ^{56}Ni masses, ^{56}Ni distributions, and kinetic energies. The dependency of the color distribution on each parameter is investigated, and it is found that helium-rich progenitors can explain SNe Ib, and helium-poor progenitors can explain SNe Ic well. In conclusion, it is expected that SNe Ib and Ic have different chemical structures and different degrees of ^{56}Ni mixing.

Keywords: supernova: general – stars: massive – methods: numerical simulation

Student Number: 2019-22292

Contents

List of Figures

List of Tables

Chapter 1

Introduction

1.1 Supernovae

Supernovae (SNe) are explosions of stars in their last evolutionary stage. The phenomenon has multifaceted implications in astronomy. It marks the endpoint of stellar evolution and releases heavy elements, contributing to the chemical evolution of the universe. SNe inject momentum and energy into the surroundings, thus regulating star formation in the host galaxy. Some types of SNe can be used as an extragalactic distance measure thanks to their standardizable characteristic. Since SNe entail energetic phenomena such as shock and neutrino emission, SNe have been a great testing ground for high energy physics. SNe provide one of the most important constraints for the theory of stellar evolution.

The classification of SN is primarily based on its spectral features (Figure 1.1). At its optical maximum, Type I SN shows no H I line while Type II SN shows H I lines. Type I SN is further divided into Type Ia, the spectrum of which shows strong Si II 6150Å line but no He I line, Type Ib which shows He I lines and no Si II line, and Type Ic which lacks both He I lines and Si II lines. SN whose spectrum has the characteristics of Type II at first but transforms into Type Ib is termed as Type IIb

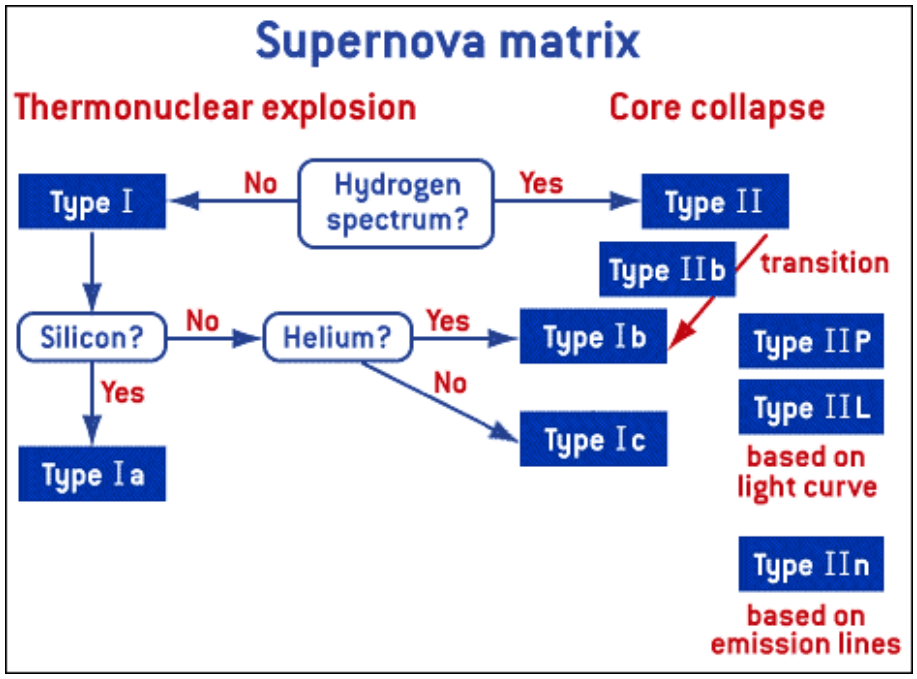

Figure 1.1 Schematic illustration of supernova classification. Credit: Rick Johnson

SN. Type II is subtyped based on the shape of its light curve; Type II-P shows a long plateau phase, and Type II-L shows a linearly declining light curve. Type IIn is used to refer to SNe which show narrow Hα emission lines.

Two mechanisms are responsible for most of the SN explosion: thermonuclear explosion and core-collapse explosion. Thermonuclear explosion occurs in degenerate carbon-oxygen white dwarfs, which originate from low- and intermediate-mass stars. When a white dwarf accretes mass from its companion, and its mass exceeds the Chandrasekhar mass (approximately $1.4M_{\odot}$), it undergoes explosive nuclear burning. The explosion disrupts the whole star, leaving no compact remnant. Type Ia SNe, known for their standardizable characteristic (Philips relation; Phillips 1993), belong to this category.

On the other hand, core-collapse explosion occurs in massive stars ($M \gtrsim 8M_{\odot}$).

When the iron core reaches the Chandrasekhar mass, the core collapses. As the core reaches nuclear density, the infalling matter encounters a sharp increase in pressure, and an outward shock wave is created. The shock accumulates energy through neutrinos created by electron captures and photo-disintegration processes occurring in the core while undergoing standing accretion shock instability. Then, the shock expels the matter and finally unbinds the star. There is another possibility of a rotation-powered explosion that requires magnetar or collapsar as a central engine. The explosion leaves either a neutron star or a black hole as a remnant. Most SN subtypes other than Type Ia are caused by this mechanism.

1.1.1 Type Ib and Type Ic supernova

Type Ib and Type Ic supernovae (SNe Ib/Ic) are referred to as stripped-envelope SNe since they both lack H I lines, which indicates the deprivation of their hydrogen envelope. Their progenitors are assumed to be Wolf-Rayet stars (Yoon et al. 2017), in which strong stellar wind causes the loss of hydrogen envelope, or a binary star, in which binary interactions strip off the hydrogen envelope (Yoon et al. 2010).

The evolutionary paths towards SNe Ib/Ic progenitors involve the intertwined effects of binarity, rotation, metallicity, mass-loss, etc. By comparing model predictions with SN observations, we can constrain stellar evolution theories. For example, binary progenitors give final masses of $M_{\rm f} \approx 1.4 - 6M_{\odot}$ which are more compatible with the ejecta masses estimated from observations ($M_{\rm ej} = 1 - 6M_{\odot}$) than Wolf-Rayet progenitors (Yoon 2015). Rotation and metallicity also play an important role in a mass-loss history, which determines pre-SN structures, the properties of which dictate photometric and spectroscopic properties of SNe Ib/Ic. Thus, exploring the properties of SNe Ib/Ic comprise an important branch of understanding massive star evolution, and for this, correct inferences of progenitor natures from the observable parameters should be preceded.

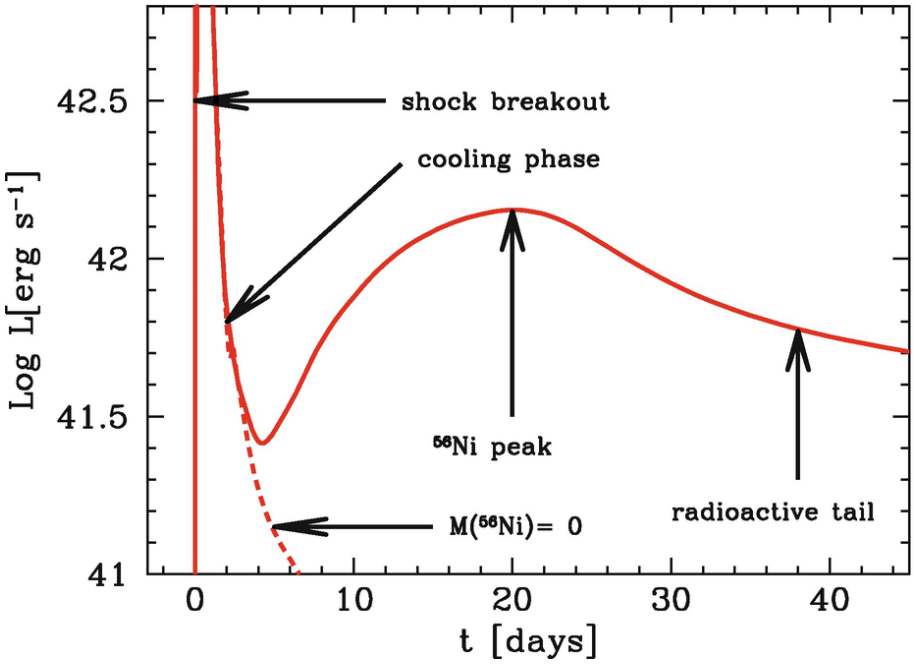

Figure 1.2 General light curve of Type I supernova. From Bersten M.C., Mazzali P.A. (2017).

1.2 Light curve and color properties of Type I supernova

General features of Type I SN light curves at early days are captured in Figure 1.2. After the explosion, shock propagates through the ejecta and emerges at the surface of the star (shock breakout). At the shock cooling phase, shock-heated ejecta emits radiation while undergoing quasi-adiabatic expansion. At this stage, the main energy source is the thermal energy deposited by the shock. Then, ^{56}Ni radioactive decay powers the light curve. After the peak, it shows a radioactive tail from the remaining radioactive material. The optical depth of the ejecta at $0 \sim 40$ day is $\tau \gtrsim 1$, so the photosphere can be defined. This phase is usually referred to as the photospheric phase, used to be distinguished from the subsequent nebular phase, in which the

optical depth of the entire ejecta is $\tau < 1$. Our concern is in the photospheric phase.

The most widely-used semi-analytic light curve model is the Arnett's model (Arnett 1982). It assumes homologous expansion, constant opacity, central concentration of ^{56}Ni, and separability of temporal and spatial parts of the thermal structure to explain the ^{56}Ni-powered phase ($5 \sim 40$ d in Figure 1.2). The maximum brightness appears at $t_{\rm max} \propto \kappa^{1/2} M_{\rm ej}^{3/4} E_k^{-1/4}$ after the explosion, and its peak luminosity reads $L_{\rm max} \propto M_{\rm Ni}\left[{\rm s_{Ni}e^{-t_{max}/\tau_{Ni}}} + {\rm s_{Co}e^{-t_{max}/\tau_{Ni}}}\left({\rm e^{-t_{max}/\tau_{eff}}} - 1\right)\right]$ where κ is the constant opacity, $M_{\rm ej}$ is the ejecta mass, E_k is the kinetic energy, $M_{\rm Ni}$ is the mass of ^{56}Ni, $s_{\rm Ni}$ is the specific energy release of ^{56}Ni, and $s_{\rm Co}$ is the specific energy release of ^{56}Co. In SNe Ib/Ic, typical values of the peak are $t_{\rm max} \sim 15 - 20$ day and $L_{\rm max} \sim 10^{42} - 10^{43}{\rm ergs}^{-1}$ (Taddia et al. 2015). Despite the simplifications, the model is being used as a convenient tool to infer SN properties.

Color and its evolution is a useful probe of SN properties as well. The $B-V$ color evolution of SNe Ib/Ic in the early days can be used to infer the ^{56}Ni distribution in the ejecta (Yoon et al. 2019). The early-time color evolution with a strong outward ^{56}Ni mixing shows monotonic reddening while that with a weak ^{56}Ni mixing shows initial reddening, blueward evolution, and reddening, in turn. Color can also be used to estimate the host galaxy reddening. The methods include using homogeneity in $V - R$ at 10 days after the R-maximum (Drout et al. 2011) and intrinsic color template between 0 d to +20 d relative to $B-$band maximum (Stritzinger et al. 2018).

1.3 This Thesis

In this thesis, the nature of SNe Ib/Ic progenitors is probed by investigating the light curves and color evolution. This was conducted by using the numerical simulation code, STELLA. STELLA is a multi-group radiation hydrodynamics code for SN explosion, which can resolve the earliest evolution of the physical properties until

SN reaches the homologous stage. In the first study (Chapter 2), the effects of circumstellar matter on SNe Ic light curve and color evolution are explored. We focus on three SNe Ic, LSQ14efd, iPTF15dtg, and SN 2020bvc which show bright post-breakout emission in the optical bands and present the best-fit models. In the second study (Chapter 3), the optical color difference between SNe Ib and Ic is discussed. We construct progenitor models with different chemical structures to explain the color difference.

Chapter 2

The Effect of Circumstellar Matter on the Double-peaked Type Ic Supernovae and Implications for LSQ14efd, iPTF15dtg and SN 2020bvc[1]

Abstract

Double peaked light curves are observed for some Type Ic supernovae (SNe Ic) including LSQ14efd, iPTF15dtg and SN 2020bvc. One possible explanation of the first peak would be shock-cooling emission from massive extended material around the progenitor, which is produced by mass eruption or rapid expansion of the outermost layers of the progenitor shortly before the supernova explosion. We investigate the effects of such circumstellar matter (CSM) on the multi-band optical light

[1]The contents of this chapter was submitted to the Astrophysical Journal and is under review

curves of SNe Ic using the radiation hydrodynamics code STELLA. Two different SNe Ic progenitor masses at the pre-SN stage (3.93 $M_{\odot}$ and 8.26 $M_{\odot}$) are considered in the SN models. The adopted parameter space consists of the CSM mass of $M_{\rm CSM} = 0.05 - 0.3 M_{\odot}$, the CSM radius of $R_{\rm CSM} = 10^{13} - 10^{15}$ cm and the explosion energy of $E_{\rm burst} = (1.0 - 12.0) \times 10^{51}$ erg. We also investigate the effects of the radioactive nickel distribution on the overall shape of the light curve and the color evolution. Comparison of our SN models with the double peaked SNe Ic LSQ14efd, iPTF15dtg and SN 2020bvc indicate that these three SNe Ic had a similar CSM structure (i.e., $M_{\rm CSM} \approx 0.1 - 0.2 M_{\odot}$ and $R_{\rm CSM} = 10^{13} - 10^{14}$ cm), which might imply a common mechanism for the CSM formation. The implied mass loss rate of $\dot{M} \gtrsim 1.0\ M_{\odot}\ {\rm yr}^{-1}$ is too high to be explained by the previously suggested scenarios for pre-SN eruption, which calls for a novel mechanism.

2.1 Introduction

Mass loss from stars can occur through multiple channels like standard radiation-driven steady winds, pulsation-driven winds, episodic eruptions and binary interactions. Mass-loss has a great influence on the evolution of massive stars and the resultant core-collapse supernova (SN) types (e.g., Smith 2014). While the progenitors of Type II SNe (SNe II) have a considerable amount of hydrogen in their envelopes, the progenitors of Type Ib and Ic SNe (SNe Ib/Ic) are supposed to be Wolf-Rayet (WR) stars or naked helium stars of which the hydrogen envelopes have been stripped off via mass loss (e.g., Yoon 2015).

If strong mass loss occurred shortly before a SN explosion, it would create a thick layer of circumstellar matter (CSM) around the SN progenitor. The interaction of such a CSM layer and the SN ejecta would have a significant impact on the SN light curve and spectra. The most notable examples are the interacting supernovae like SNe IIn and SNe Ibn (e.g., Blinnikov 2017; Smith 2017; Moriya et al. 2018). Many

recent studies on ordinary SNe IIP also report evidence for the presence of massive CSM around the progenitors (e.g., González-Gaitán et al. 2015; Khazov et al. 2016; Förster et al. 2018). This implies that a large fraction of SN IIP progenitors would undergo strong enhancement of mass loss at the pre-SN stage, for which various mechanisms have been proposed in the literature (e.g., Yoon et al. 2010; Quataert & Shiode 2012; Woosley & Heger 2015; Fuller 2017).

Compared to the case of SN IIP progenitors that are mostly red supergiants, SNe Ib/Ic progenitors are compact and would need more energy for mass ejection. However, some recent theoretical studies predict a significant mass loss enhancement at the pre-SN stage from helium star progenitors by wave heating (Fuller & Ro 2018), rapid rotation (Aguilera-Dena et al. 2018) or silicon flashes (Woosley 2019)[2]. This would be related to the narrow emission lines of SNe Ibn and the unusually bright early-time emission of some SNe Ib including SN 2008D and LSQ13abf.

The presence of massive CSM might also be responsible for the first peak of several double-peaked superluminous SNe Ic (e.g., LSQ14bdq; Nicholl et al. 2015; Nicholl & Smartt 2016) and peculiar SNe Ic like SN 2006aj (e.g., Modjaz et al. 2006), iPTF15dtg (Taddia et al. 2016, 2019) and SN 2020bvc (Ho et al. 2020; Rho et al. 2020). The magnetar scenario is often invoked to explain such an unusual SN Ic. Given that rapid rotation is a necessary condition for the production of a magnetar, rotationally-driven rapid mass loss during the final evolutionary stage might commonly occur for magnetar progenitors (Aguilera-Dena et al. 2018). Alternatively, the double peak feature could be explained by the magnetar model where the shock driven by the magnetar energy breaks out the already expanding SN ejecta (Kasen et al. 2016).

[2]The pulsational pair-instability from very massive helium stars ($34 \lesssim M_{\rm He} \lesssim 62\ M_{\odot}$; Woosley 2017) is another possibility for strong mass ejection at the pre-SN stage. But in the present study, our discussion only focuses on relatively low-mass helium star progenitors that would undergo core-collapse having a final mass less than about 10 $M_{\odot}$.

On the other hand, no double-peaked light curve has been found for most of the ordinary SNe Ic that are powered by radioactive ^{56}Ni. To our knowledge, the SN Ic LSQ14efd is the only ordinary SN Ic (in terms of energy, ejecta and nickel mass; see below) that shows a signature of the double peaked light curve (i.e., bright post-breakout emission; Barbarino et al. 2017). Given that strong pre-SN mass loss would be a likely reason for this double peak feature and that the mass loss mechanism might be different from the case of the magnetar-powered SNe, it would be worth investigating the effect of CSM on the early-time light curves of SNe Ic to infer the physical properties of the CSM around the LSQ14efd progenitor and to provide a theoretical constraint for future observations of SNe Ic. For this purpose, we present multi-color SN Ic light curve models calculated with the radiation hydrodynmics code STELLA considering a thick CSM environment around the progenitor and apply the results to LSQ14efd, of which the photometric data are given by Barbarino et al. (2017).

Although our original motivation is to explain the optical light curve of LSQ14efd, we also apply our results to two other double peaked SNe Ic: iPTF15dtg and SN 2020bvc. Intriguingly, we find that these double-peaked SNe Ic of our sample had similar CSM properties in terms of CSM mass and radius, which might imply a common mechanism of pre-SN mass ejection.

In Section 2, we describe the SN Ic progenitor models, the considered parameter space and the numerical method. In Section 3, we show the effects of different parameters of CSM on the light curves and color evolution of SNe Ic. In Section 4, we apply our result to LSQ14efd, iPTF15dtg, and SN 2020bvc, and discuss its implications for the mass loss mechanism. In Section 5, we present our conclusions.

Table 2.1 Progenitor model properties

Model	M	R	$m_{\rm He,env}$	$Y_{\rm s}$	$M_{\rm Fe}$	$E_{\rm bind}$
	$[M_\odot]$	$[R_\odot]$	$[M_\odot]$		$[M_\odot]$	10^{51} erg
4P	3.93	0.77	0.06	0.49	1.44	0.3
8P	8.26	0.25	0.08	0.15	1.85	1.5

Note. — M: total mass of the progenitor model; R: Radius; $m_{\rm He,env}$: integrated helium mass for the region above the iron core; Y_s: surface helium abundance; $M_{\rm Fe}$: iron core mass that corresponds to the adopted mass cut; $E_{\rm bind}$: binding energy.

2.2 Modeling

Our progenitor models for the SN simulations are helium poor stars with final masses of 3.93 $M_\odot$(4P model) and 8.26 $M_\odot$(8P model) and their properties are given in Table 2.1. These models are obtained by evolving helium stars of 7.0 $M_\odot$ and 15 $M_\odot$ at the initial metallicity $Z_{\rm init} = 0.02$, respectively, with the MESA code (Paxton et al. 2011, 2013, 2015, 2018). Here we adopt step-overshooting with an overshooting parameter of $0.1H_P$ where H_P is the local pressure scale height at the outer boundary of the helium burning convective core. We use the Wolf-Rayet mass-loss rate prescription by Nugis & Lamers (2000) until core helium exhaustion and a fixed mass-loss rate of 10^{-4} $M_\odot$ yr^{-1} during the later evolutionary stages. The total amounts of helium retained in the outer region above the iron core are only 0.06 $M_\odot$ and 0.08 $M_\odot$ in 4P and 8P models respectively, and therefore these models are suitable for SNe Ic rather than SNe Ib. See also Figure 2.1 for the chemical composition of the progenitor models.

To calculate the SN models, we use the one-dimensional multi-group radiation hydrodynamics code STELLA (Blinnikov et al. 1998, 2000, 2006; Blinnikov & Tol-

stov 2011). It solves a set of time-dependent radiative transfer equations coupled with the hydrodynamics equations. The covered wavelength range in the calculations is $5 \times 10^4 - 10^{-3}$ Å, for which 109 wavelength bins are used. The ionization levels and excitation levels are obtained with the assumption of local thermodynamic equilibrium. Both scattering and absorption are considered in the opacity treatment (Blinnikov et al. 1998; Kozyreva et al. 2020). The effects of fluorescence and non-LTE that are not included in STELLA would affect the light curve especially when the radioactive ^{56}Ni is present near the photosphere (see Blinnikov et al. 1998, for a detailed discussion). For example, fluorescence would possibly make the SN color bluer than our model prediction when the light curve is dominated by ^{56}Ni heating. However, these effects only play a minor role in the early-time light curve dominated by the shock cooling emission from the interaction between CSM and SN ejecta, which is the main concern of this study. Multi-dimensional effects might also affect the precise determination of SN parameters. The full description of fluorescence, non-LTE effects as well as multi-dimensional effects will be available in a future version of STELLA (Potashov et al. 2017; Panov et al. 2018).

The SN explosion is treated as a thermal bomb at the mass cut, which corresponds to the iron core mass in this study (see Table 2.1). Our progenitor models are mapped into the STELLA code and 250 mass zones including 80 zones in the CSM are used for SN simulations. Readers are referred to Blinnikov & Tolstov (2011) and references therein for details of the STELLA code and to Yoon et al. (2019) for a recent example of the use of STELLA for modeling SNe Ib/Ic.

2.2.1 Nickel distribution

We do not calculate the explosive nucleosyntheis, which is not the subject of this work, and instead put a certain amount of radioactive ^{56}Ni in the input progenitor models. We assume a nickel distribution which follows a Gaussian profile as in Yoon

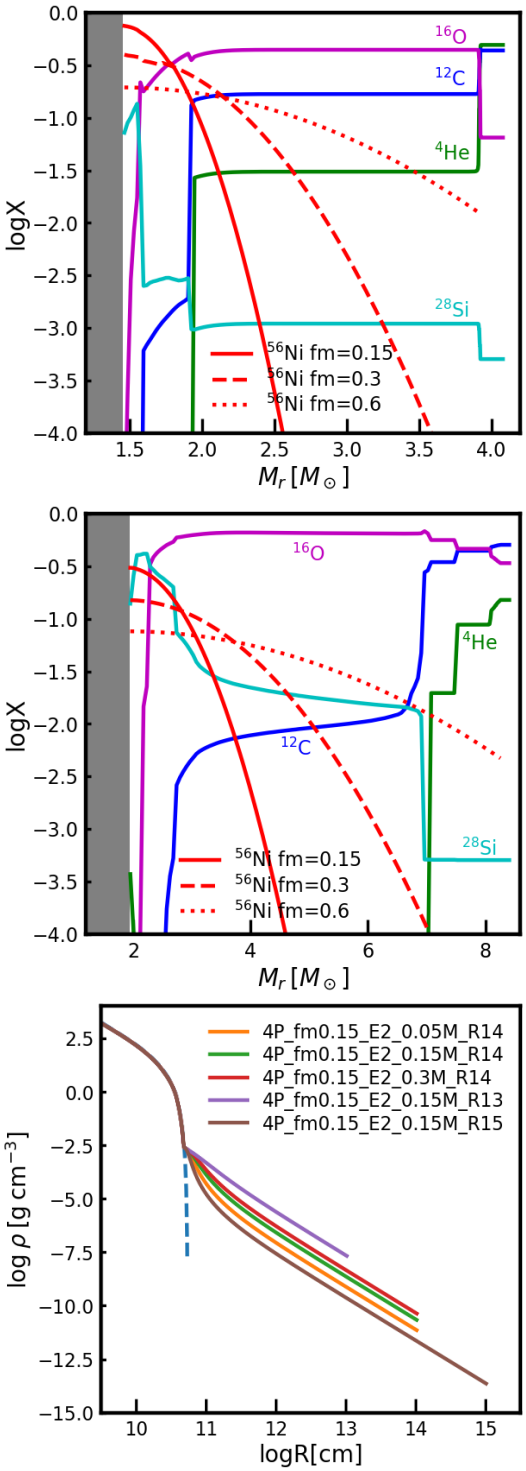

Figure 2.1 Chemical compositions of a 4P model (top) and a 8P model (middle) with the same nickel distribution parameter, $f_{\rm m}$= 0.15. For comparison, nickel profiles with different $f_{\rm m}$ are also shown on the figure. Density profiles of a representative set of 4P models with different CSM structure (bottom). The dashed line shows the density profile of the original 4P progenitor.

et al. (2019):

$$X_{\rm Ni}(M_r) = A\exp\left(-\left[\frac{M_r - M_{\rm Fe}}{f_{\rm m}(M_{\rm tot} - M_{\rm Fe})}\right]^2\right). \quad (2.1)$$

Here, A is the normalization factor, M_r the mass coordinate, $M_{\rm Fe}$ the iron core mass, $M_{\rm tot}$ the total mass of the progenitor, and $f_{\rm m}$ the ^{56}Ni distribution parameter. For our fiducial models, we fix the total ^{56}Ni mass to 0.25 $M_\odot$, which is the inferred value for LSQ14efd (Barbarino et al. 2017). This amount of ^{56}Ni is within the typical range of the ^{56}Ni mass distribution of ordinary SNe Ic (Anderson 2019). We calculate SN models using different values of $f_{\rm m}$, which determines the degree of ^{56}Ni mixing in the SN ejecta: the ^{56}Ni distribution becomes flatter for a larger $f_{\rm m}$ and vice versa as shown in Figure **??**fig:ini.

2.2.2 CSM structure

We assume that the CSM has the density profile of $\rho_{\rm CSM} = \dot{M}/4\pi v_{\rm wind} r^2$, with the standard β-law wind velocity profile: $v_{\rm wind}(r) = v_0 + (v_\infty - v_0)\left(1 - \frac{R_0}{r}\right)^\beta$. Here $\dot{M}$ is the mass-loss rate of the progenitor, v_0 is the wind velocity at the progenitor surface, v_∞ is the terminal velocity, R_0 is the radius of the progenitor, and r is the distance from the center of the progenitor. The density profile would follow r^{-2} after the wind is accelerated in a transition layer. According to Fuller & Ro (2018), hydrogen-poor stars are predicted to emit wave-driven outbursts with terminal velocities of a few 100 km s^{-1}. We fix the terminal velocity to 200 km s^{-1} in this study. Note that there exists degeneracy between $\dot{M}$ and v_∞: a larger v_∞ would imply a larger $\dot{M}$ for a given CSM mass, which should be kept in mind when we discuss our result.

For the wind velocity parameter β, we assume $\beta = 3.0$. Although this value can affect the early-time light curves of Type IIP supernovae significantly (Moriya et al. 2018), our SN Ic models depend on β very weakly because of the small radii of the progenitors. The CSM mass can vary by a factor of 5 to 500 for $\beta = 1 \cdots 5$ for red supergiant SN progenitors (Moriya et al. 2018) but only by 3% for our models.

Besides, we assume that the chemical composition of the CSM follows that of the outermost part of the progenitor. It would be possible that the CSM is more helium-rich than the progenitor surface. However, our test calculations indicate that the early-time light curves are not meaningfully affected for our considered parameter space even if a helium-rich composition is adopted, although it might be important for the details of early-time spectra.

In the bottom panel of Figure 2.1, the density profile of the 4P progenitor is presented with the blue dashed line. The density decreases very steeply near the surface of the progenitor. The SN shock is rapidly accelerated in this region, making the time step very small. To avoid this numerical difficulty, we take off $4 \times 10^{-5} M_{\odot}$ of the outermost layer of the progenitor when we attach CSM in our models. As discussed below (Section 2.3.2), the choice of the CSM inner boundary is not important for the conclusions of this study.

Note also CSM in our models can also be considered as an extended outward moving envelope created by an energy injection during the final evolutionary stage. The difference between an outward moving envelope and wind matter would be just that an envelope is gravitationally bound to the progenitor while the wind matter is not. As long as the CSM velocity is much lower than the SN shock velocity, wind matter and an extended envelope would not lead to a difference in the resulting light curve as long as the density profile is not very much different (see Section 2.3.2).

We also calculate some models with a very small amount of CSM (0.001% of the progenitor mass) with $R = 10^{14}$ cm for comparison. In this case, the CSM would correspond to the wind material from an ordinary line-driven Wolf-Rayet wind having $\dot{M} \sim 10^{-5}\ M_{\odot}\ \mathrm{yr}^{-1}$. For convenience, these models are denoted by 'no-CSM' as the effect of CSM on the light curve is practically negligible in this case.

2.2.3 Considered parameter space

We focus on the effects of four parameters for a given progenitor mass: CSM mass ($M_{\rm CSM}$), CSM radius ($R_{\rm CSM}$), nickel distribution ($f_{\rm m}$), and explosion energy ($E_{\rm burst}$). In our fiducial models, we consider $M_{\rm CSM} = 0.05 \cdots 0.3 M_{\odot}$, $R_{\rm CSM} = 10^{13} \ldots 10^{15}$ cm, $f_{\rm m} = 0.15$, 0.3, and 0.6. We consider the explosion energy of $E_{\rm burst} = (1 \cdots 3) \times 10^{51}$ erg. for 4P models and $E_{\rm burst} = (5 \cdots 12) \times 10^{51}$ erg for 8P models. The ^{56}Ni mass is set to 0.25 $M_{\odot}$ and 0.40 $M_{\odot}$ for reproducing the main peaks of LSQ14efd/iPTF15dtg and SN 2020bvc, respectively.

For simplicity, each model is referred to as xP_$f_{\rm m}$_$E_{\rm burst}$_ $M_{\rm CSM}$_log$R_{\rm CSM}$ in the figures. For example, 4P_fm0.15 _E2_0.15M_R13 denotes the SN model with the 4P progenitor, $f_{\rm m}$=0.15, $E_{\rm burst}$=2.0B, $M_{\rm CSM}$=0.15$M_{\odot}$, and log$R_{\rm CSM}$ [cm] = 13.

2.3 Results

2.3.1 General characteristics

In STELLA, SN shock is initiated by a thermal bomb and begins to propagate outward from the assumed mass cut. The density profile is steeper than r^{-3} at the outermost layers of the progenitor (Figure 2.1) thus the shock moving forward in these layers is accelerated until it reaches the surface of the progenitor (Nadezhin & Frank-Kamenetskii 1965; Grasberg 1981; Blinnikov & Tolstov 2011). As the forward shock enters CSM, in which the density profile follows r^{-2}, it decelerates and an inward-moving reverse shock is created. These shocks convert a significant fraction of SN kinetic energy into internal energy, leading to a bright shock-cooling emission.

As an example, we present bolometric light curves of our 4P models with $f_{\rm m} = 0.15$, $E_{\rm burst} = 2.0$B, and $R_{\rm CSM} = 10^{14}$ cm for various CSM masses in Figure 2.2 and the corresponding multi-color light curves (i.e., in U, B, V, R and I bands) in Figure 2.3.

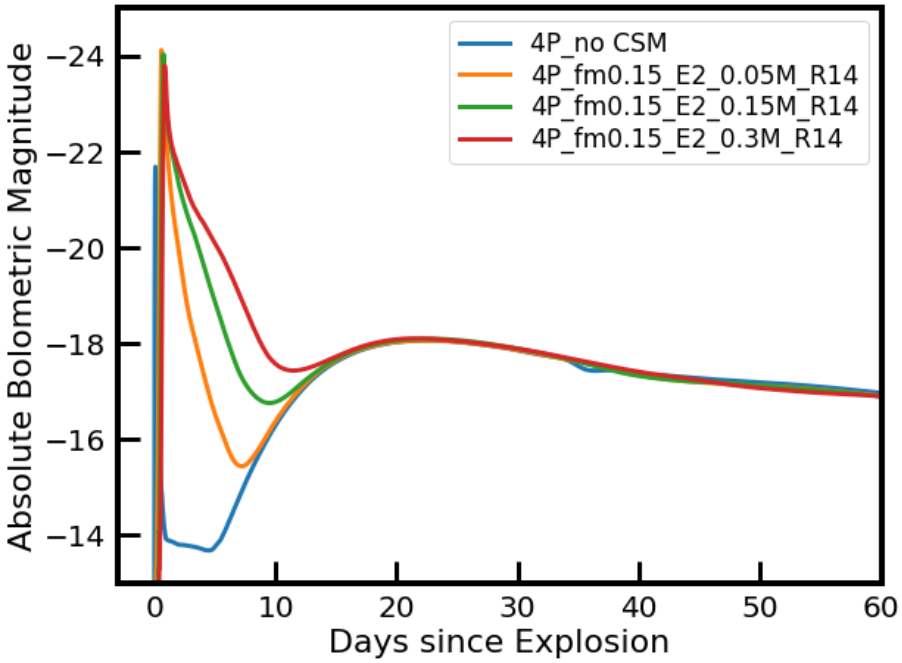

Figure 2.2 Bolometric light curves of 4P models with $f_{\rm m} = 0.15$, $R_{\rm CSM} = 10^{14}$ cm, and $E_{\rm burst} = 2$B for different CSM masses: no-CSM (blue), 0.05 $M_\odot$ (orange), 0.15 $M_\odot$ (green), and 0.30 $M_\odot$ (red brown).

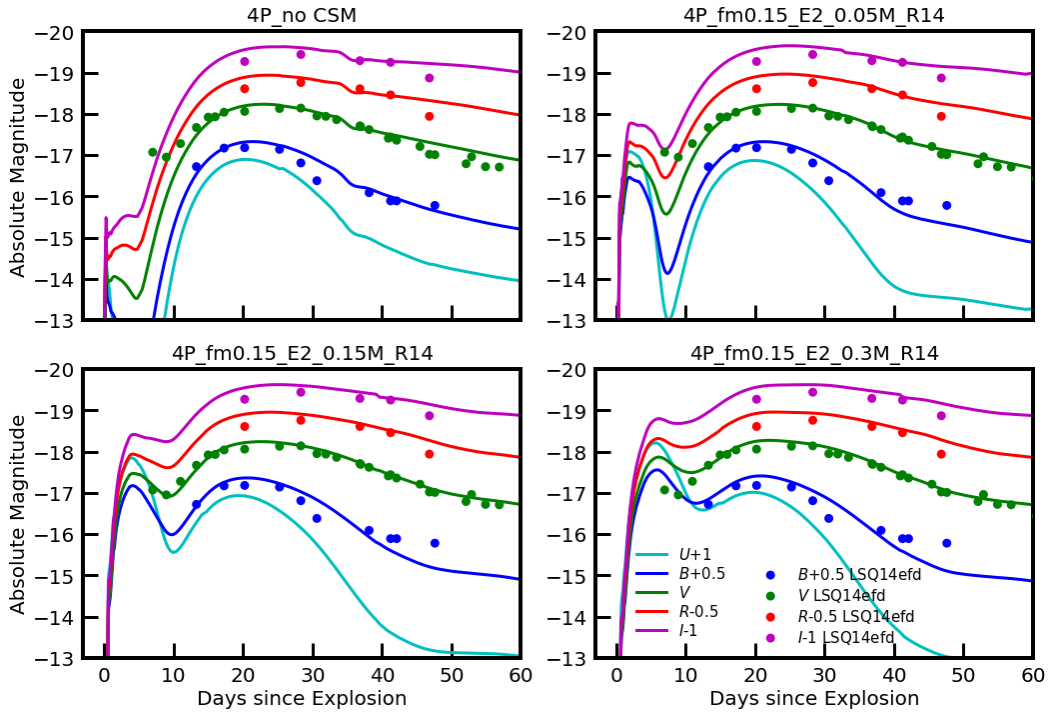

Figure 2.3 Multicolor light curves of models with and without CSM. Each panel shows models with different CSM masses. Different bands are presented using different colors as indicated by the legend in the bottom-right panel. The explosion date is chosen by mathcing the V-band light curve around the main peak with the model.

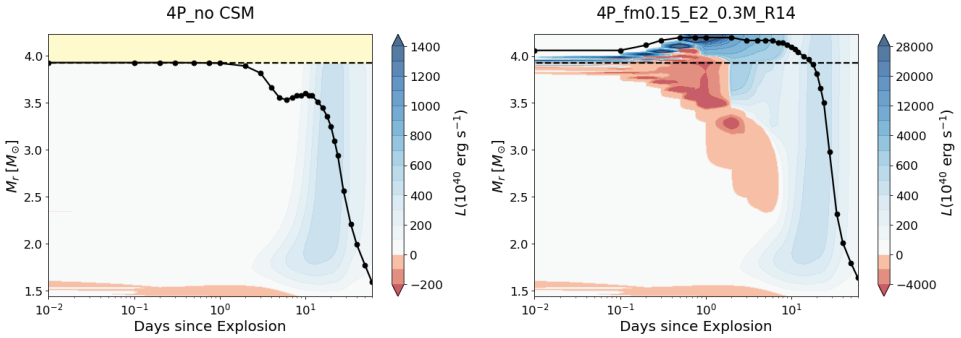

Figure 2.4 Luminosity contour maps of SN models with different CSM masses, 4P_no-CSM (left) and 4P_fm0.15_E2_0.3M_R14 (right). The points in each epoch denote the photospheres defined as the location where the Rosseland optical depth being 2/3. The dashed line represents the surface of the progenitor, which corresponds to the inner boundary of the CSM in the lower panel.

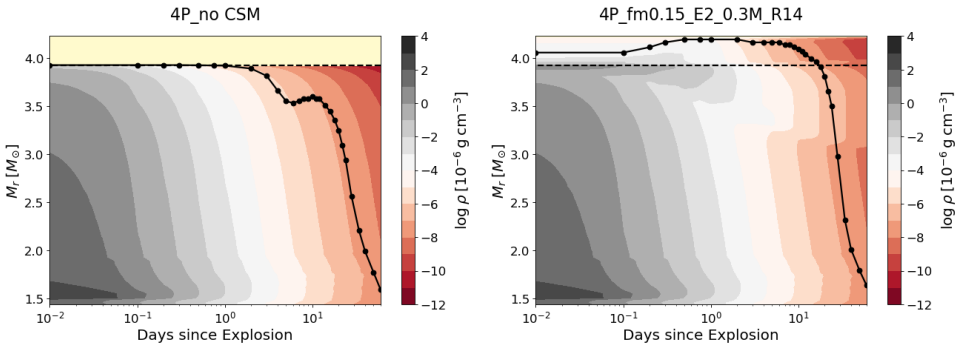

Figure 2.5 Density contour maps of SN models with different CSM masses, 4P_no-CSM (left) and 4P_fm0.15_E2_0.3M_R14 (right). The points in each epoch denote the photospheres defined as the location where the Rosseland optical depth being 2/3. The dashed line represents the surface of the progenitor, which corresponds to the inner boundary of the CSM in the lower panel.

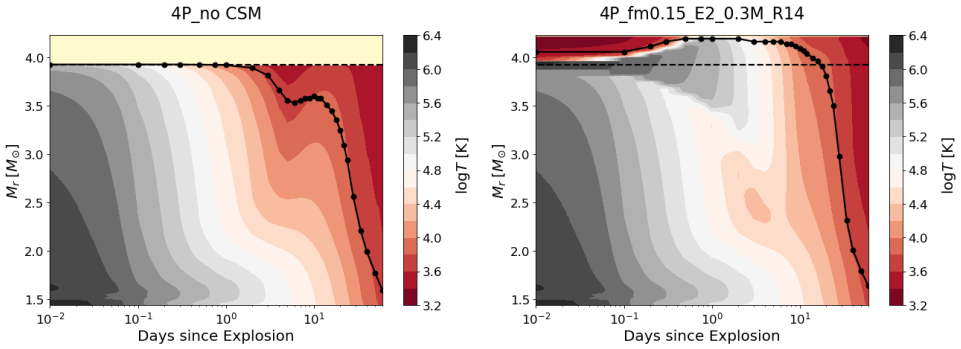

Figure 2.6 Temperature contour maps of SN models with different CSM masses, 4P_no-CSM (left) and 4P_fm0.15_E2_0.3M_R14 (right). The points in each epoch denote the photospheres defined as the location where the Rosseland optical depth being 2/3. The dashed line represents the surface of the progenitor, which corresponds to the inner boundary of the CSM in the lower panel.

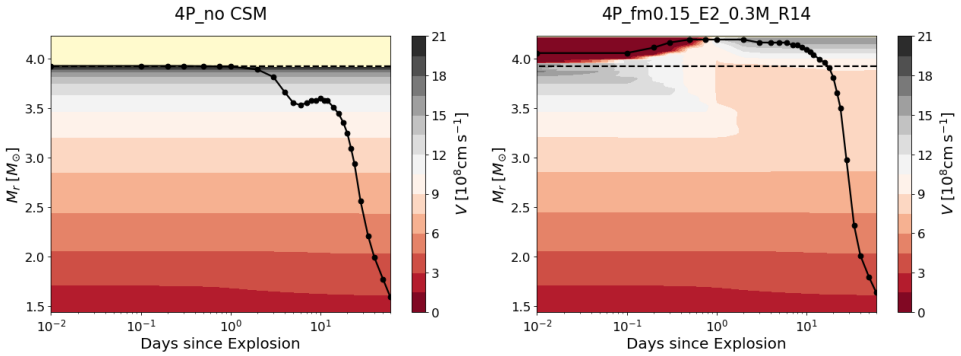

Figure 2.7 Velocity contour maps of SN models with different CSM masses, 4P_no-CSM (left) and 4P_fm0.15_E2_0.3M_R14 (right). The points in each epoch denote the photospheres defined as the location where the Rosseland optical depth being 2/3. The dashed line represents the surface of the progenitor, which corresponds to the inner boundary of the CSM in the lower panel.

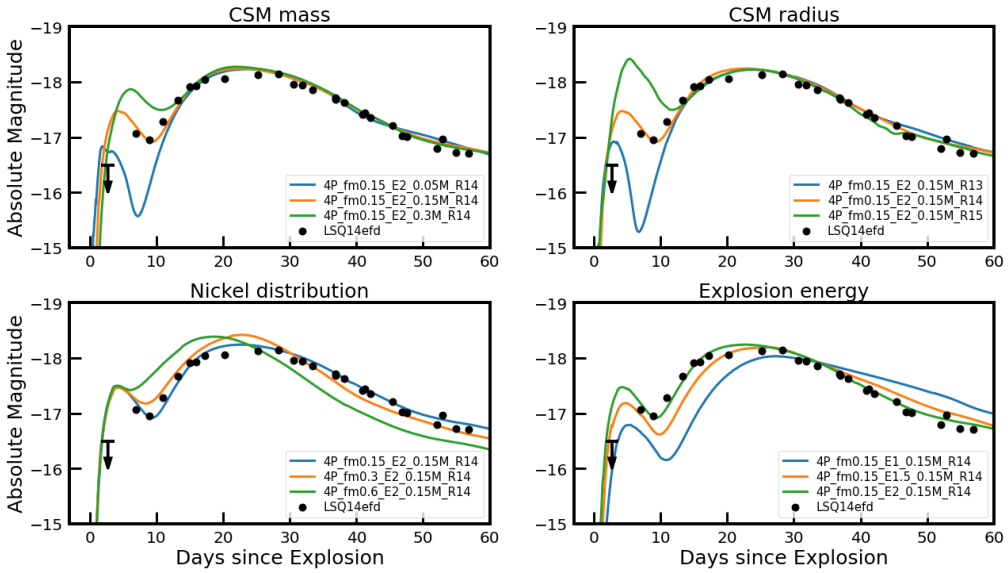

Figure 2.8 V-band light curves of 4P models. Each panel shows models with different CSM masses (upper-left), different CSM radii (upper-right), different $f_{\rm m}$ (lower-left), and different $E_{\rm burst}$ (lower-right). To see the effects of each parameter, three models were chosen respectively and drawn in solid lines as indicated by the legends in each panel. Black downward arrows indicate the pre-explosion limit. The explosion date is chosen by matching the observed V-band light curve around the main peak with our fiducial model 4P_fm0.15_E2_0.15M_R14.

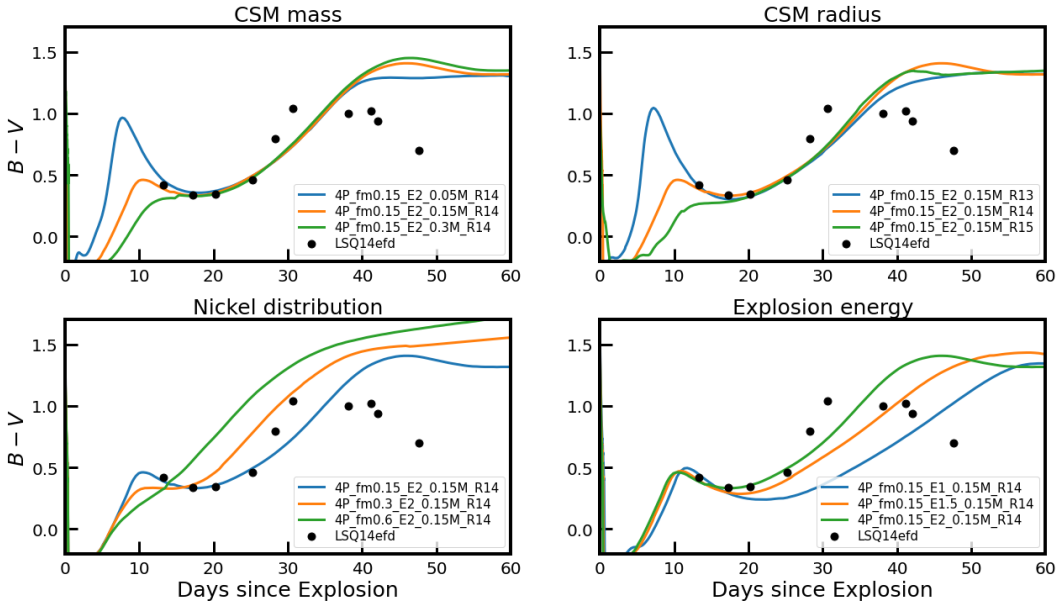

Figure 2.9 Evolution of the $B-V$ color of the 4P SN models presented in Figure 2.8. Each panel shows the models with different CSM masses (upper-left), different CSM radii (upper-right), different $f_{\rm m}$ (lower-left), and different $E_{\rm burst}$ (lower-right). To see the effects of each parameter, three models were chosen respectively and drawn in solid lines as indicated by the legends in each panel.

.

After the shock breakout, the bolometric luminosity of the no-CSM model drops very rapidly until the post-breakout plateau phase is reached (See Dessart et al. 2011, for a detailed discussion on this short-lived plateau phase of SNe Ib/Ic). By contrast, for the models with CSM, it remains brighter and decreases more slowly for several days (e.g., $\sim$ 10 days for $M_{\rm CSM} = 0.15 M_{\odot}$). The main power source during this period is the interaction of the SN shock and the CSM. We refer to this period as the 'interaction-powered phase (IPP)' following Moriya et al. (2011). After the IPP, the light curve is dominated by the energy due to the radioactive decay of ^{56}Ni, and we refer to this phase as the '^{56}Ni-powered phase (NPP)'.

To better understand the role of CSM in the IPP, we compare the evolution of the local luminosity (L_r), density (ρ_r), temperature (T_r) and velocity (v_r) of the 4P model having $M_{\rm CSM} = 0.3 M_{\odot}$ to those of the no-CSM 4P model in Figures 2.4, 2.5, 2.6 and 2.7. In the CSM model, the propagation of the forward and reverse shocks can be traced by the positive and negative luminosity peaks in the bottom panel of Figure 2.4. No aftereffect of the shocks is seen for the no-CSM model since there is barely an interplay of the shock and the wind matter.

The location of the photosphere is also greatly affected by the presence of CSM. As seen in Figure 2.5, in the CSM model the photosphere (defined by the Rosseland mean opacity) initially moves upward in the CSM in the mass coordinate until $t \simeq 1.0$ d. The photosphere gradually moves downward thereafter along with the SN ejecta expansion.

The shocked layers are heated up and the outermost layers in the CSM model remain much hotter than in the no-CSM model from $t = 0.6$ d when the forward shock breaks out the CSM (Figure 2.6). These shocked layers in the CSM model have a significantly lower velocity compared to the no-CSM model (Figure 2.7). Note also that a dense shell is formed at $M_r \approx 3.2 - 3.9 M_{\odot}$ as the reverse shock sweeps up this region.

These effects of the shock become more prominent for a larger CSM mass; a larger amount of the kinetic energy is transformed into the internal energy as more layers are shock-heated and decelerated. Furthermore the lower expansion velocity makes the expansion cooling less efficient and the photon diffusion time longer. These factors make the IPP longer and the bolometric and optical luminosities during the IPP brighter for a larger CSM mass as seen in Figures 2.2 and 2.8.

The CSM also has a great impact on the SN color. Given that the photosphere during the IPP is hotter for a larger CSM mass, the color of the SN during the IPP becomes bluer as seen in Figure 2.9 (see the upper left panel).

Yoon et al. (2019) showed that, without CSM, the early-time color evolution of a SN Ib/Ic sensitively depends on the ^{56}Ni distribution in the SN ejecta. Stronger mixing of ^{56}Ni into the outermost layers would lead to a bluer color in the earliest days followed by a monotonic reddening during the photospheric phase, while fairly weak mixing leads to three distinct phases of initial reddening, blueward evolution, and reddening again. In addition, a strong ^{56}Ni mixing tends to suppress the post-breakout emission that would otherwise appear during early times (Dessart et al. 2012; Piro & Nakar 2013; Yoon et al. 2019). Our CSM models in Figures 2.9 indicate, however, that a monotonic reddening can also be realised with a sufficient amount of CSM (e.g., for the cases of 4P_fm0.15_E2_0.3M_R14 and 4P_fm0.15_E2_0.15M_R15 in Figure 2.9), even if the ^{56}Ni mixing is weak (i.e., $f_{\rm m} = 0.15$).

On the other hand, the heat due to ^{56}Ni in the inner region diffuses outward while the photosphere moves down toward the ^{56}Ni-heated region as can be seen in Figure 2.4. Once the luminosity is dominated by this ^{56}Ni heating, the IPP ends and the NPP begins. The light curve during the NPP is determined by the total ^{56}Ni mass and its distribution and becomes almost independent of the CSM structure (Figures 2.2 and 2.8).

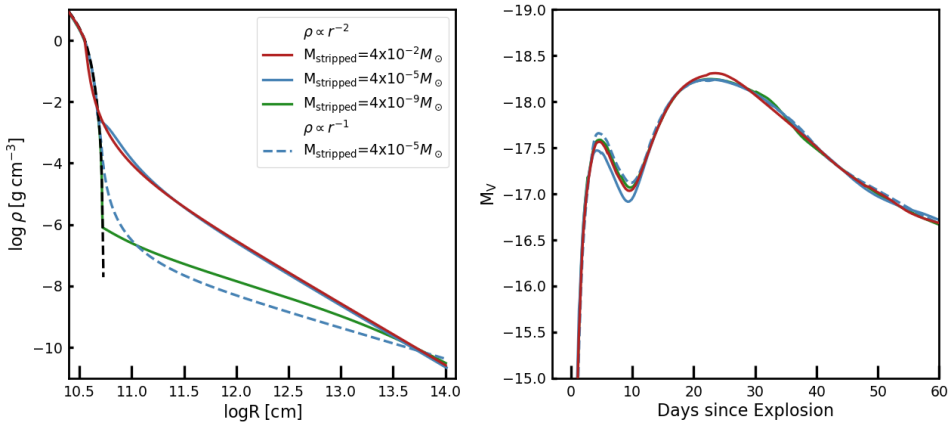

Figure 2.10 Density profiles of models with different $M_{\rm stripped}$ (i.e., different choices of the boundary between the progenitor star and the CSM; see the text for details) and density profile laws (left) and the corresponding V-band light curves (right). All other parameters are same with our fiducial 4P_fm0.15_E2_0.15M_R14 model. Solid lines correspond to models with different $M_{\rm stripped}$ with $\rho \propto r^{-2}$ while the blue dashed line corresponds to the model with $\rho \propto r^{-1}$ and $M_{\rm stripped} = 4 \times 10^{-5}\ M_\odot$, as indicated by the legends in the left panel. In the left panel, the original progenitor density profile is given by the black dashed line for comparison.

2.3.2 The effects of various parameters

Density profile

The CSM density profile is uncertain. If the CSM was created by a radiation-driven steady wind, it would follow the standard wind density profile which converges to r^{-2} at sufficiently large r. If the mass ejection were driven by energy injection from an inner region of the star, the outermost layers where the binding energy is lowest would be lifted up to make an outward-moving envelope-like structure. Here we discuss the effect of CSM density profile on the result.

As explained above, in our fiducial model we remove a tiny amount of mass (i.e.,

$M_{\rm stripped}$=4×10^{-5} $M_\odot$) from the outermost layers of the progenitor star and attach the CSM of $\rho(r) \propto r^{-2}$. We have tested how this choice affects the light curve by adopting different $M_{\rm stripped}$ and $\rho(r)$ as shown in the left panel of Figure 2.10. The total amount of the CSM mass is same for all different cases (i.e., $M_{\rm CSM} = 0.15\ M_\odot$).

As shown in the right panel of Figure 2.10, the difference in $M_{\rm stripped}$ by several orders of magnitude only leads to a $\sim$0.2 mag difference in the V-band light curve during the IPP. A test model with CSM density profile of $\rho \propto r^{-1}$ also gives the practically same light curve as the fiducial case of $\rho \propto r^{-2}$. The differences are negligible compared to the effect of different CSM mass and radius in our parameter space. Therefore, the details of a steady-wind-like structure having $\rho \propto r^{-n}$ with $1 \leq n \leq 2$ play a less important role in the light curve compared to the CSM mass and radius. It should be kept in mind, however, that a very different density structure (e.g., a shell-like structure) might yield a significantly different result during the IPP and that our calculations would not give a unique solution for the CSM mass and radius.

CSM radius

We present V-band light curves and $B-V$ color evolution of 4P models with $f_{\rm m}$ = 0.15 and $E_{\rm burst}$ = 2B in the upper panels of Figures 2.8 and 2.9, respectively, for different combinations of $M_{\rm CSM}$ and $R_{\rm CSM}$. It is seen that a larger CSM radius leads to a brighter emission and a bluer color during the IPP for a given set of $M_{\rm CSM}$, $f_{\rm m}$ and $E_{\rm burst}$. For $M_{\rm CSM} = 0.15 M_\odot$, the IPP peak magnitudes of $M_V = -16.9, -17.5, -18.4$ are achieved for $\log R_{\rm CSM}$[cm] = 13, 14, and 15, respectively. This is because a less amount of the kinetic energy is consumed for the expansion work for a more extended CSM.

It seems that there exists a certain degree of degeneracy between $M_{\rm CSM}$ and $\log R_{\rm CSM}$ with regard to the IPP brightness: a different set of these parameters

could result in a similar IPP peak magnitude. For example, in Figure 2.8, the V-band IPP peak of the 4P models with $M_{\rm CSM} = 0.05$ and $\log R_{\rm CSM}[{\rm cm}] = 14$ looks fairly comparable to the case with $M_{\rm CSM} = 0.15$ and $\log R_{\rm CSM}[{\rm cm}] = 13$ (i.e., $M_V \sim -16.8$). However, the rise time to the IPP peak becomes longer for a larger $M_{\rm CSM}$ mass: $t_{\rm rise} = 3.0$ d for $M_{\rm CSM} = 0.15$ and $\log R_{\rm CSM}[{\rm cm}] = 13$ and $t_{\rm rise} = 1.9$ d for $M_{\rm CSM} = 0.05$ and $\log R_{\rm CSM}[{\rm cm}] = 14$. Therefore, in principle, the degeneracy between $M_{\rm CSM}$ and $\log R_{\rm CSM}$ could be broken, as discussed below in Section 2.4.1.

Distribution of ^{56}Ni

The IPP and the NPP in the light curve can be clearly distinguished if there exists a sufficient time gap between the two phases. This time gap becomes shorter as ^{56}Ni is more mixed out to the outer layers of the ejecta, which makes the ^{56}Ni heating important at an earlier time and the luminosity at the local minimum of the light curve between the two phases higher (the bottom-left panel of Figure 2.8). For example, in the models of the figure, the NPP starts 5 d and 2 d after the IPP peak and the magnitude difference between the IPP peak and the local minimum is 0.6 mag and 0.1 mag for $f_{\rm m} = 0.15$ and 0.6, respectively. Therefore, the ^{56}Ni mixing is also an important parameter that can significantly interfere the IPP in the light curve.

In addition, the overall properties of the NPP are greatly influenced by the ^{56}Ni mixing (e.g., see Yoon et al. 2019, for a more detailed discussion). For example, the NPP peak is reached earlier with a larger $f_{\rm m}$. In the 4P models presented in Figure 2.8, it peaks at $t = 18$ d for $f_{\rm m} = 0.6$, and at $t = 22$ d for $f_{\rm m} = 0.15$.

In the color evolution, the effect of ^{56}Ni mixing on models with CSM is qualitatively same with the case of no-CSM, which is discussed in detail by Yoon et al. (2019). As mentioned above, a very strong ^{56}Ni mixing results in a monotonic reddening (e.g., the case for $f_{\rm m} = 0.6$ in the bottom-left panel of Figure 2.9). A

monotonic reddening is also observed with a sufficiently large CSM mass (e.g., the case for $M_{\rm CSM} = 0.3 M_{\odot}$ in the top-left panel of Figure 2.9), even when the ^{56}Ni mixing is weak (i.e., $f_{\rm m} = 0.15$). However, the color during the NPP is mostly much redder in the former case, for which the ^{56}Ni abundance and the resultant opacity at the photosphere are higher.

Explosion energy

As the explosion energy increases for a given progenitor, the rise time and the duration of the IPP become shorter (the bottom-right panel of Figure 2.8). The time spans between two points at +0.5 mag from the IPP peak are 6.4 d, 6.2 d, 6.0 d, respectively for E1.5, E2, E2.5 model shown in the figure. This is because the expansion velocity of the SN ejecta is faster, making thermal diffusion more efficient. Also, the luminosity gets higher during the IPP since a stronger shock creates a hotter and denser shocked shell. On the other hand, the higher velocity of the SN ejecta with a higher explosion energy makes the opacity decrease more quickly, which in turn makes the recession of the photosphere to the ^{56}Ni heated reagion faster. This results in the earlier appearance of the ^{56}Ni peak for a larger explosion energy as 27.3 d, 26.2 d, 23.7 d for the same above models, followed by a steeper decline as 0.032 mag/d, 0.043 mag/d, 0.047 mag/d during 30 days from the NPP peak.

In terms of color, no significant difference during the IPP is found for different explosion energies in the 4P models (the bottom-right panel of Figure 2.9). Although the local peak of $B - V$ at the transition between the IPP and the NPP ($\sim$ 10 d) are similar, the blueward evolution, which marks the beginning of the NPP, begins somewhat earlier for a higher explosion energy. Besides color tends to redden more quickly after the NPP peak because of the faster ejecta cooling.

Progenitor mass

To explain the light curve width around the NPP peak of the LSQ14efd, we need $E_{\rm burst} \simeq 1.5 - 2.0$B and $E_{\rm burst} \simeq 5.0 - 8.0$B for the 4P and 8P models (Figures 2.8 and 2.11). The corresponding kinetic energies are $E_{\rm K} \simeq 1.2 - 1.7$B and $E_{\rm K} = 3.5 - 6.5$B, respectively. The higher explosion energies of the 8P models than the 4P models result in a steeper rise to the IPP peak as well as a steeper decrease from it. For our fiducial model, 4P model with $M_{\rm CSM} = 0.15 M_{\odot}$, $f_{\rm m} = 0.15$, $E_{\rm burst} = 2$B and $\log R_{\rm CSM}[{\rm cm}] = 14$, the slope of the V-band light curve towards the IPP peak (from +0.5 mag before the peak to the peak) and the slope beyond the peak (from the peak to the +0.5 mag after the peak) is -0.25 mag/d and 0.11 mag/d. For the corresponding 8P model with $E_{\rm burst} = 8$B, the slopes towards the peak and beyond the peak are -0.43 mag/d and 0.14 mag/d, respectively. The IPP peaks in the V-band of all 8P models are brighter by ~ 0.5 mag than the 4P models for a given set of the parameters.

The higher explosion energies make all $B-V$ colors of 8P models redden faster during the IPP and hence the local peak of $B-V$ at the transition between the IPP and the NPP larger than in the corresponding cases of 4P models. For the 8P models presented in Figure 2.12, the local $B-V$ peak at the IPP to NPP transition (~ 13 d) is larger by about 0.7 mag than for the corresponding 4P models (see Figure 2.9).

On the other hand, the color during the NPP is significantly affected by ^{56}Ni heating. The adopted ^{56}Ni mass is the same for 4P and 8P models (hence the same amount of ^{56}Ni heating energy) but the ejecta mass of the 8P models is 2.6 times higher than the 4P models (see Table 2.1). As a result, the 8P models are significantly redder during the NPP than the corresponding 4P models. At the NPP peak, for example, the $B-V$ values of the 8P models are larger by about 0.5 mag than the corresponding 4P models.

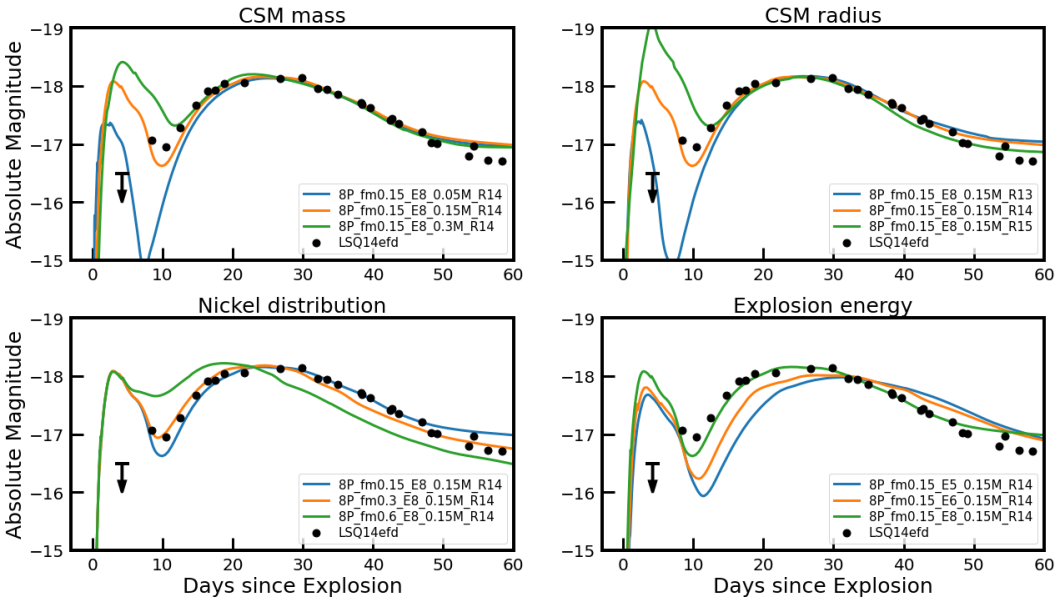

Figure 2.11 Same as in Figure 2.8 but for the 8P SN models. The explosion date is chosen by matching the observed V-band light curve around the main peak with the model 8P_fm0.15_E8_0.15M_R14.

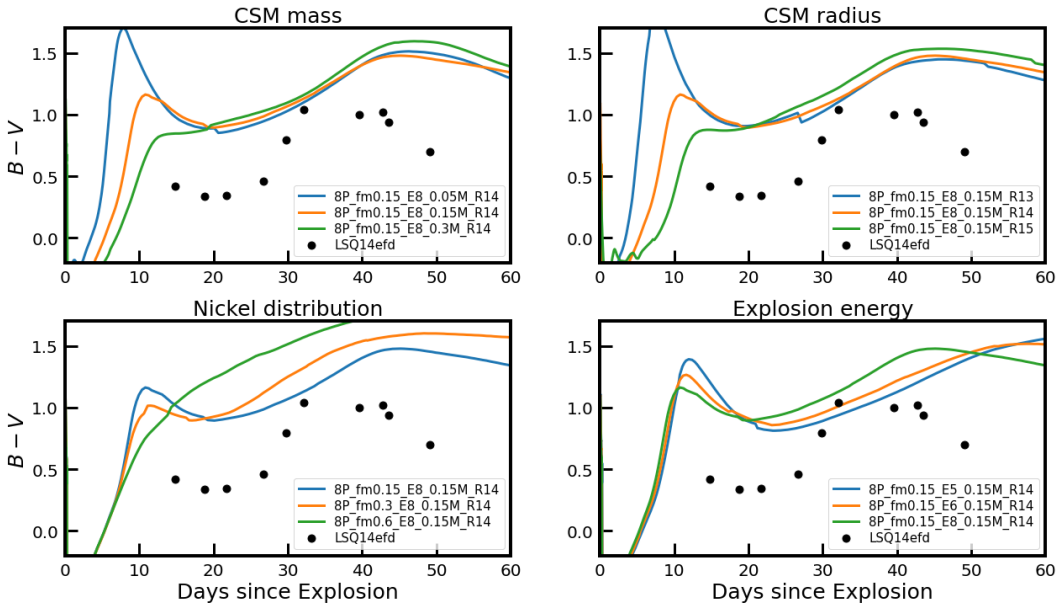

Figure 2.12 Same as in Figure 2.9 but for the 8P SN models presented in Figure 2.11.

2.4 Applications to double peaked SNe Ic

2.4.1 LSQ14efd

In this section, we apply our results to the SN Ic LSQ14efd, which motivated this work. The comparison of our SN models with the observation is done with eyes. The observed data are taken from Barbarino et al. (2017). Although a quantitative fitting procedure (Morozova et al. 2018; Ergon et al. 2015) is also possible with our grid of models, eye inspection is more than enough because our grid resolution is rather coarse, as can be seen in Figures 2.8 and 2.11.

For the comparison of the models with the observation, the distance modulus of 37.1 is adopted for LSQ14efd. Given that we have only one data point of the IPP of this SN, the explosion date cannot be easily determined from the observation. In Figures 2.8 and 2.11, the explosion date is chosen from the model that can best reproduce the V-band light around the NPP peak. The corresponding explosion

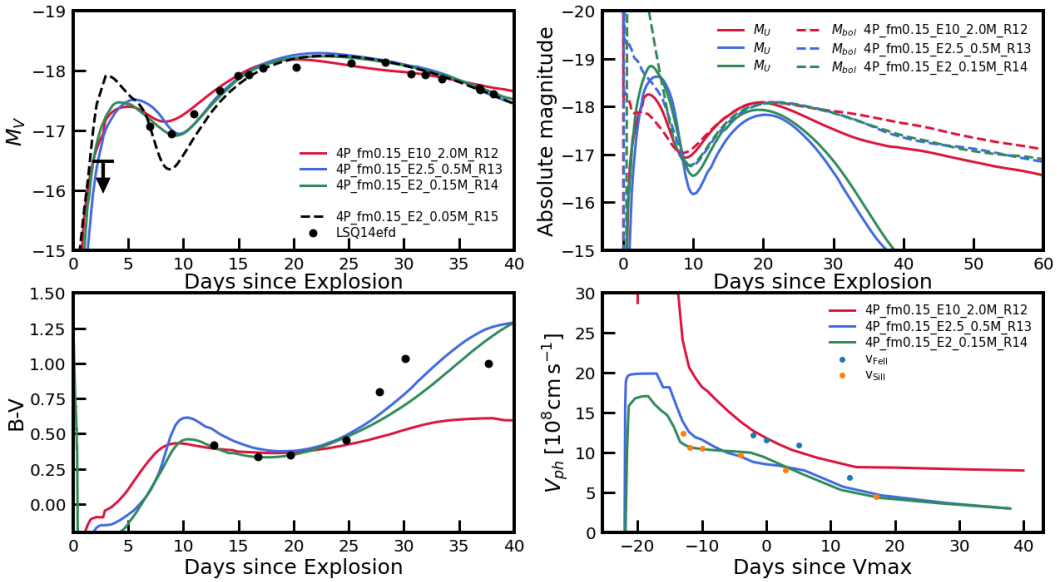

Figure 2.13 *Upper left:* V-band light curves of some SN models with different CSM structures (see the labels in the figure) compared to the observed V-band light curve of LSQ14efd. *Lower left*: the corresponding $B-V$ color evolution. *Upper right:* U-band and bolometric light curves of the models. *Lower right:* Photospheric velocity of the models compared with the FeII and SiII line velocities of LSQ14efd.

dates are MJD 56875.5 d and 56874.0 d for 4P and 8P models, respectively. However, when we make eye inspection to find the best fit model, we freely shift the explosion date such that the light curve around the V-band NPP peak of each model may match the observation.

As can be seen in Figures 2.3 and 2.8, non-detection with the upper magnitude limit of $m_{\rm V} = 20.6 \pm 0.2$ at 22 d before the V-band maximum is reported for this SN (Barbarino et al. 2017). The information about the IPP peak and its rise time is missing and only one data point before the end of the IPP is available in the V-band (i.e., $m_V = 20.03$ at $t = 56882.48$ MJD; the first observed point). The local minimum in the V-band at the trasition between IPP and NPP ($t = 56884.44$ MJD; the second observed point) is $m_V = 20.15$. The data in the other optical bands are available only after the IPP.

To find the model parameters that can give a consistent fit to LSQ14efd, we take the following steps. First, the amount of ^{56}Ni is fixed to 0.25 $M_\odot$, which is inferred from the NPP peak brightness (Barbarino et al. 2017), as explained above. Second, we only use the models with $f_{\rm m} = 0.15$ because the color evolution of these models is qualitatively same as that of LSQ14efd where the signature of relatively weak ^{56}Ni mixing is found (see the discussion in Section 2.3.2).

For the remaining sets, we search for the CSM parameters (i.e., $\log R_{\rm CSM}$ and $M_{\rm CSM}$) that can best explain the three data points of the observed IPP (i.e, the non-detection limit, the first observed point, and the second observe point which is the local minimum at the IPP to NPP transition; see Figure 2.8) as well as $E_{\rm burst}$ that can give a reasonable V-band light curve width compared to LSQ14efd.

We find that no 8P model can satisfy the non-detection limit: given the very high energies (i.e,. $E_{\rm burst} = 6.0$B and 8.0B), too bright emission is predicted at the point of non-detection for the models that can match the second and third data points of the IPP (see Figure 2.11). Note also that the color predicted by the 8P models is

much redder than the observation (i.e., by more than 0.6 mag at the NPP peak in terms of $B-V$; Figure 2.12).

Within the grid of our fiducial 4P models with $f_{\rm m}=0.15$, we find that the IPP brightness can be best reproduced by the model with $M_{\rm CSM}=0.15M_{\odot}$, $R_{\rm CSM}=10^{14}$ cm and $E_{\rm burst}=2.0$B. This best fit model is presented in Figure 2.13 (the green line). The model with $R_{\rm CSM}=10^{15}$ cm which can well reproduce the first observed point is also shown in the figure for comparison (the dashed line). This model predicts too faint emission at the second point of the observed IPP, and can be ruled out.

As discussed in Section 2.3.2, different combinations of $M_{\rm CSM}$ and $R_{\rm CSM}$ can yield a similar IPP peak. To investigate this uncertainty, in Figure 2.13, we also present two test models for which we adopt $M_{\rm CSM}=2.0M_{\odot}$ and $R_{\rm CSM}=10^{12}$ cm (the red line) and $M_{\rm CSM}=0.5M_{\odot}$ and $R_{\rm CSM}=10^{13}$ cm (the blue line). These models and our best fit model have a similar IPP peak in V-band. However, the evolution after the IPP peak is different for each case. The model with $M_{\rm CSM}=2.0M_{\odot}$ and $R_{\rm CSM}=10^{12}$ cm have a very long term effect of CSM and predicts brighter emission at the second and third observed points. The $B-V$ color evolution of this model after the NPP peak is also distinctively different from the observation. The model with $M_{\rm CSM}=0.5M_{\odot}$ and $R_{\rm CSM}=10^{13}$ cm has a longer decline rate from the IPP peak than our best fit model and predict too bright emission compared to the observation at the first observed point.

We find that the degeneracy between $M_{\rm CSM}$ and $R_{\rm CSM}$ could be more easily broken in the U band as seen in the upper right panel of Figure 2.13. The compared tree models have a similar IPP peak in the V band but the U band IPP peak is systematically brighter for a larger $R_{\rm CSM}$, for which the adiabatic cooling is less efficient. Therefore, U-band observations during early times would be most useful in future observational studies on the CSM properties.

In principle, the degeneracy between $M_{\rm ej}$ and $E_{\rm K}$ which exists when inferring SN parameters with a NPP light curve can be broken by comparing the photospheric velocity and the model prediction. As seen in Figure 2.13, the photospheric velocity evolution of our best fit model is consistent with the observed $v_{\rm SiII}$. Barbarino et al. (2017) use $v_{\rm FeII}$, which is higher than $v_{\rm SiII}$, to infer SN parameters and as a result obtain higher $M_{\rm ej}$ and $E_{\rm K}$ (i.e., 6.3 $\rm M_\odot$ and 5.6B) than our fiducial values. However, as discussed above, such a high SN energy of 5.6B is not favored when the observed IPP is compared with the models. In our models, the photosphere is defined by the Rosseland mean opacity and it would be an interesting subject of future work to investigate which absorption line better traces the Rosseland mean photosphere.

We conclude that the early-time light curve of LSQ14efd is consistent with the SN model prediction with a massive CSM of about $M_{\rm CSM} \approx 0.15 M_\odot$ extending up to about $R_{\rm CSM} \approx 10^{14}$ cm. This corresponds to a mass loss rate of $\dot{M} \approx 1.0 M_\odot$ yr^{-1} during ~ 0.2 yr before the SN explosion if we assume the terminal wind velocity as 200 km s^{-1}. We discuss its implications for the mass loss mechanism below in Section 2.4.3.

2.4.2 iPTF15dtg and SN 2020bvc

We also compare our models with two other double peaked SNe Ic SN iPTF15dtg and SN 2020bvc. iPTF15dtg is a peculiar SN Ic which is suspected to be powered by a magnetar (Taddia et al. 2019) and its optical light curves around the main peak cannot be easily explained by our grid of models. Given that our main interest is to infer the properties of CSM, here we do not attempt to make a model that can reproduce the NPP (see instead Taddia et al. 2016, who inferred SN parameters from the light curve around the main peak). As discussed above, the IPP light curve is largely determined by $M_{\rm CSM}$, $R_{\rm CSM}$ and $E_{\rm burst}$, which can be fairly well determined independently of the detailed properties of the NPP if the early time data of the

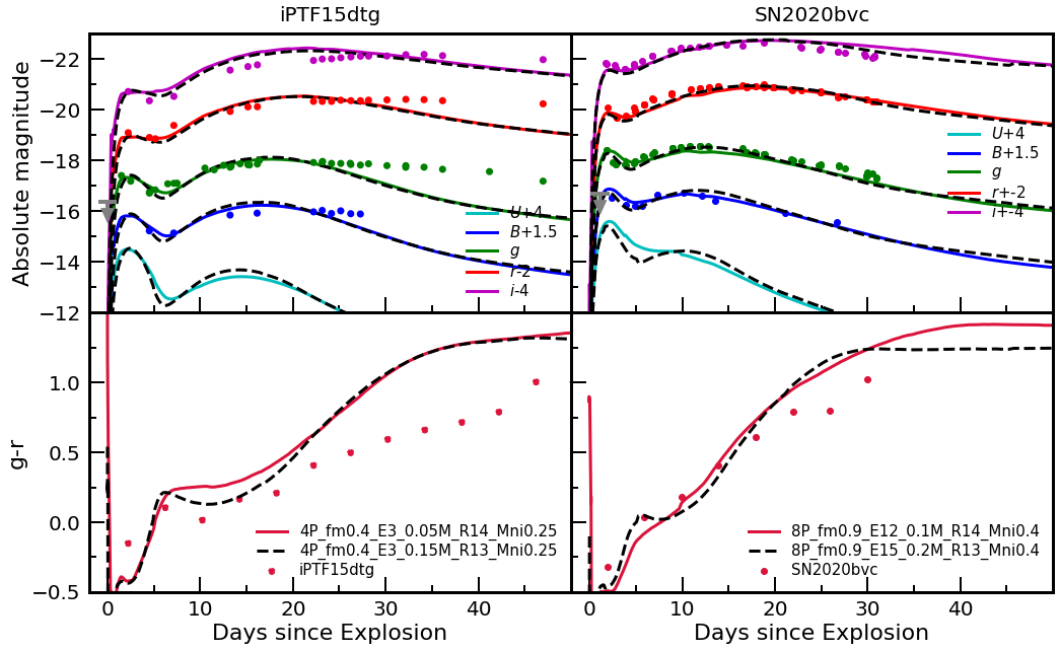

Figure 2.14 Light curves and color evolution of iPTF15dtg and SN2020bvc overlapped with the best-fit models. In the upper panels, solid lines and dashed lines represent R14 models and R13 models, respectively. Bottom panels show $g-r$ color evolution of the same models. $g-r$ of each SN is obtained from linear interpolation of each band magnitude. Photometric data and extinction correction of iPTF15dtg were imported from The Open Supernova Catalog and Taddia et al. (2016), and SN2020bvc from Ho et al. (2020). For iPTF15dtg, the explosion date is chosen to be MJD 57332.9 d, the last non-detection date. For SN 2020bvc, it is chosen by matching the observed V-band light curve around the main peak with our best fit model. Grey downward arrows indicate the pre-explosion limit in g-band.

IPP are good enough.

Comparison of our model grid with the IPP light curve of this SN indicates that the early-time light curve ($0 \sim 15$ d after the explosion) of iPTF15dtg is fairly consistent with two of our 4P models: 4P_fm0.4_E3_0.05M_R14 and 4P_fm0.4_E3_0.15M_R13, as seen in Figure 2.14. Here, the last non-detection date is chosen for the explosion date since we cannot fit the main peak with our grid of models. This implies that the progenitor of iPTF15dtg had CSM with $R_{\rm CSM} = 10^{13} - 10^{14}$cm and $M_{\rm CSM} = 0.05 - 0.15 M_{\odot}$.

For SN 2020bvc, we already presented a result of our model comparison with the observation in another paper (Rho et al. 2020). For this particular SN, we use the 8P progenitor and assume that ^{56}Ni is uniformly distributed in the inner 90% of the SN ejecta. The ^{56}Ni mass required to explain the NPP peak is found to be 0.4 $M_{\odot}$. As in the case of LSQ14efd, the explosion date is determined by matching the observed V-band light curve around the main peak with the models. For the properties of these models made for the comparison with SN 2020bvc, see Table A.3. Within our grid, we find that the overall light curve properties including the IPP of SN 2020bvc are most consistent with the following two sets of parameters: $M_{\rm CSM} = 0.1 M_{\odot}$, $R_{\rm CSM} = 10^{14}$ cm & $E_{\rm burst} = 12$ B, and $M_{\rm CSM} = 0.2 M_{\odot}$, $R_{\rm CSM} = 10^{13}$ cm & $E_{\rm burst} = 15$ B. The early-time color of this SN is very blue as predicted by the model, which is due to the SN interaction with CSM.

2.4.3 Implications for the CSM formation mechanism

Our result indicates that the inferred CSM properties of the double peaked SNe Ic considered in this study (LSQ14efd, iPTF15dtg and SN 2020bvc) are intriguingly similar: $M_{\rm CSM} \approx 0.1 - 0.2 M_{\odot}$ and $R_{\rm CSM} \approx 10^{13} - 10^{14}$ cm.

The implied mass loss rate is $\dot{M} \approx 0.6 - 13.0$ $(v_{\rm w}/200$ km s$^{-1})$ $M_{\odot}$ yr^{-1}. The mass eruption should have occurred within about 0.2 yr from the explosion if we

adopt $v_{\rm w} = 200$ km s^{-1}.

This high mass loss rate inferred in our study cannot be explained by the conventional line-driven wind of Wolf-Rayet stars. Fuller & Ro (2018) explore the possibility of pre-supernova outbursts via wave heating during core neon and oxygen burning in a 5 $M_\odot$ hydrogen-free helium star. The predicted mass loss rate is $\sim 0.01 M_\odot$ yr^{-1} with a wind terminal velocity of a 450 km s^{-1}. This is smaller by two or three orders of magnitude than our inferred value. Note also that helium-poor SN Ic progenitor stars are supposed to be more compact by several factors than helium-rich SN Ib progenitors which are considered by Fuller et al. (e.g., Yoon et al. 2019). Therefore, it seems that the inferred CSM property of the double peaked SNe Ic cannot be easily explained by the wave heating model.

Aguilera-Dena et al. (2018) find that the surface layers of helium stars could be spun-up to the critical rotation during the final evolutionary stages if the helium stars retained sufficiently high angular momenta. The predicted mass loss rate is about $\dot{M} \lesssim 0.01 M_\odot$ yr^{-1} during the last years of the evolution, which is also much lower than our inferred mass loss rate.

Woosley (2019) find that very massive CSM of $0.02 \cdots 0.74$ $M_\odot$ can be created by silicon flash for helium stars having initial helium star masses of 2.5 - 3.2 $M_\odot$. However, all these He star models with silicon flash have a fairly massive helium envelope ($> 0.7 M_\odot$) and the resulting SN would be a SN Ib rather than SN Ic. In addition, the silicon flash only occurs for a relatively small progenitor mass (i.e, $M_{\rm final} \lesssim 2.6 M_\odot$), which could not easily explain the light curves of the double peaked SNe Ic of our sample.

One scenario that could explain the CSM of the double peaked SNe Ic of our sample would be the possibility that the mass loss from the progenitor was induced by the combined effects of wave heating and rotation. If the progenitor were rotating at the critical rotation during the core neon and oxygen burning stages, the binding

energy of the outermost layers would be lower than the non-rotating case and the mass loss due to the wave heating would be easier.

This scenario is in line with the fact that iPTF15dtg and SN 2020bvc belong to peculiar SNe Ic (ie., magnetar-powered/broad-lined SNe Ic), for which a rapid rotating progenitor is often invoked. This might also imply that the LSQ14efd progenitor was a rapid rotator even though the inferred properties of LSQ14efd do not look peculiar except for the IPP signature. It is possible that LSQ14efd was in part powered by a mangetar, in which case the actual ^{56}Ni would be smaller than the inferred value of 0.25 $M_{\odot}$.

Another possibility is that the progenitors did not really undergo a mass eruption, but simply an expansion of the outer layers due to an energy injection during the pre-SN stage. Althernatively, the IPP observed in our sample might not be related to CSM, but to interactions with a companion star (Kasen 2010) or to high velocity ^{56}Ni due to an asymmetric explosion (e.g., Folatelli et al. 2006; Bersten et al. 2013). An elaboration of these scenarios would be a subject of future work.

2.5 Conclusions

We have discussed the effects of CSM on the early-time SNIc light curve and color evolution. SN models with different CSM mass, CSM radius, fm, and Eburst are investigated in a systematic fashion to understand the IPP properties. In Table A.1, we present the IPP properties of the investigated SN models for $f_{\rm m}$=0.15, which can be summarized as follows.

1. Models with more massive CSM have brighter IPP peaks in the optical bands for a given initial condition. For example, for all 4P models given in Table A.1, the V-band peak during the IPP gets higher by -0.32mag when CSM mass increases by $0.1M_{\odot}$ (values obtained by linear regression) due to efficient con-

version of kinetic energy into thermal energy (Section 2.3.1). At the same time, the rising time ($t_{\rm rise}$) and the light curve width ($\Delta t_{+0.3}$) get extended by 1.61 d and 1.19 d due to a longer diffusion time scale.

2. The CSM radius has the same qualitative effect on IPP properties as the CSM mass. Models with a larger CSM radius consume less energy due to the expansion work thus making the IPP brighter (Section 2.3.2). For example, 4P model in Table A.1 gets brighter by -0.13 mag when its CSM radius increases by 10^{14} cm. It also makes the rising time and the width of the IPP longer, by 0.20 d and 0.16 d.

3. A higher explosion energy makes the IPP brighter and its time scale shorter (Section 2.3.2). For our 4P models, the IPP peaks higher by -0.63 mag, the rising time and the IPP duration are shortened by -1.28 d and -0.96 d when their explosion energy is increased by 1B, respectively. However, it has a negligible effect on the color evolution during the IPP for a given explosion condition within our considered parameter space.

4. The IPP can be significantly interfered by ^{56}Ni heating if ^{56}Ni mixing is sufficiently strong (Section 2.3.2). In particular, the local brightness minimum between IPP and NPP becomes larger and the time span between the IPP and NPP peaks shorter with a stronger ^{56}Ni mixing.

5. The early-time color becomes significantly bluer with CSM compared to the case without CSM.

We compare our models with three double-peaked SNe Ic LSQ14efd, iPTF15dtg and SN 2020bvc. We find that the inferred CSM properties of these SNe Ic are intriguingly similar: a CSM mass of $M_{\rm CSM} =\sim 0.1 M_{\odot}$ and a CSM radius of $R_{\rm CSM} = 10^{13} - 10^{14}$ cm. This possibly suggests a common mechanism for the CSM formation from the progenitors of these SNe Ic. The implied mass loss rate of $\dot{M} \gtrsim$

1.0 $M_{\odot}$ yr^{-1} ($v_{\rm w}$/200 km/s) seems to be too high to be explained by the existing theories such as wave heating or rotationally-induced mass shedding (Section 2.4.3). Future work needs to address if there exists a possible mechanism to explain such massive extended material around the progenitor star, or if an alternative scenario such as asymmetric explosion might explain the bright IPP of the double peaked SNe Ic of our sample.

Chapter 3

Optical Color of Type Ib/Ic Supernovae and Implications for their Progenitors

Abstract

Type Ib and Type Ic supernovae (SNe Ib/Ic) originate from hydrogen-deficient progenitors; however, it is still not in consent whether SN Ic progenitors are helium-rich like SN Ib progenitors. Using the archived SN data, we investigate optical color of SNe Ib/Ic and show that SNe Ib are systematically bluer than SNe Ic at the optical maximum. We construct SN models from helium-rich and helium-poor progenitors and find that the dichotomy in abundance structures plays an important role in making the color difference. We suggest that optical color can provide an unexplored yet meaningful photometric diagnosis of SNe Ib/Ic and can serve as evidence of their distinctively different progenitor natures.

3.1 Introduction

How different are the progenitors of Type Ib and Type Ic supernovae (SNe Ib/Ic)? - This is a long-debated subject in understanding the origin of SNe Ib/Ic. While both SNe Ib and Ic do not show any noticeable H I lines in their spectra, implying the hydrogen envelope of their progenitors is stripped off, SNe Ib show He I lines in contrast to SNe Ic. However, the lack of He I lines does not necessarily mean the lack of helium envelope in their progenitors as helium requires non-thermal processes in the line formation (Lucy 1991). This has posited a high uncertainty in determining the existence and/or amount of helium remaining in the progenitors of SNe Ic (hidden helium problem), obstructing our full comprehension of different evolutionary channels of SNe Ib/Ic until core-collapse (Yoon 2015).

Various spectroscopic analyses have been attempted to tackle the different properties between SNe Ib and Ic. The role of ^{56}Ni mixing in SN ejecta for the presence/absence of He I features was explored through non-LTE radiative transfer simulations by Dessart et al. (2012), who showed that a large amount of helium can be hidden without ^{56}Ni mixing. On the contrary, there remains yet another simple explanation that helium-rich and helium-poor stars are respective progenitors of SNe Ib and Ic. This was explored by many authors, either by investigating general features or by case studies, reproducing distinctive spectroscopic properties (Dessart et al. 2015, 2020; Hachinger et al. 2012; Teffs et al. 2020; Williamson et al. 2020). Recent statistical analysis of a large set of SNe Ib/Ic spectra seems to be in favor of the distinct progenitor structures. Stronger and broader O I λ7774 absorption line and broader Fe II λ5169 line found in SNe Ic disfavor the existence of a large amount of helium left in their progenitors (Liu et al. 2016). However, the broader spectral lines might also stem from higher degrees of ^{56}Ni mixing in SNe Ic than SNe Ib, which are predicted to make the early photospheric velocity faster (Moriya et al. 2020).

While SNe Ib/Ic spectra show distinct features, their light curves look comparable. The peak luminosity and the light curve width are related to ejecta mass, ^{56}Ni mass, and kinetic energies (Arnett 1982), and there have been many studies on light curve modeling of large samples of SNe Ib/Ic (Richardson et al. 2006; Drout et al. 2011; Cano 2013; Taddia et al. 2015; Lyman et al. 2016; Prentice et al. 2016; Taddia et al. 2018; Prentice et al. 2019; Barbarino et al. 2020). Each group used different sets of samples and inferred different average values, thus it has not reached a consensus whether SNe Ib/Ic have systematically different properties in terms of ejecta mass and ^{56}Ni mass.

A small scatter is observed in the optical color at 10 days after the optical peak (Drout et al. 2011; Stritzinger et al. 2018). However, different degrees of ^{56}Ni mixing are required to explain different features of observed SNe Ib/Ic in the early-time color evolution; SNe Ic require a stronger mixing, in favor of a He-poor star as the progenitor (Yoon et al. 2019).

In this study, we present another meaningful probe into different natures of SNe Ib/Ic progenitors: optical color at the V-band peak epoch. We show that SNe Ib are systematically bluer than SNe Ic by compiling a number of SNe Ib/Ic samples and argue that the chemical structure difference can yield such a color gap.

The paper is organized as follows. We introduce a set of observational data selected for the analysis and their optical color at the V-band peak in Section 3.2. Then we present our supernova models newly constructed for this study in Section 3.3. In Section 3.4, we compare the models with the observation and discuss the possible origins of the color difference. We conclude the study in Section 3.5.

3.2 Photometric data samples

The majority of photometric data of SNe Ib/Ic were collected from the Open Supernova Catalog (OSC) (Guillochon et al. 2017). SNe Ib/Ic which were discovered after

Table 3.1 List of our selected sample of SN Ib/Ic

Name	Type	B_{max}	V_{max}	References	$E(B-V)_{MW}$	$E(B-V)_{Host}$	References	$M_{\rm Ni}$	$M_{\rm ej}$
SN 1984I	Ib	16.65	15.82	OSC	0.091	0.104	C13	0.15	3.62
SN 1999ex	Ib	17.45	16.60	OSC	0.017	0.280	P16	0.16	2.24
SN 2004gq	Ib	15.89	15.29	OSC	0.063	0.095	P16	0.11	2.67
SN 2004gv	Ib	17.68	17.25	OSC	0.028	0.053	S18	0.15	7.04
SN 2005hg	Ib	18.08	17.51	OSC	0.089	0.580	D11	0.73	3.41
SN 2006ep	Ib	18.31	17.40	OSC	0.031	0.233	S18	0.09	1.80
SN 2006gi	Ib	17.09	16.18	OSC	0.021	0.098	E11	–	–
SN 2006lc	Ib	18.92	17.68	OSC	0.056	0.298	S18	0.20	5.12
SN 2007C	Ib	17.26	15.98	OSC	0.037	0.730	P16	0.13	3.33
SN 2007kj	Ib	18.14	17.64	OSC	0.069	0.000	T18	0.07	2.65
SN 2007Y	Ib	15.62	15.30	OSC	0.018	0.090	P16	0.04	2.12
SN 2008D	Ib	18.51	17.33	OSC	0.019	0.630	P16	0.09	4.12
SN 2009jf	Ib	15.58	15.08	OSC	0.097	0.050	P16	0.23	6.02
SN 2012au	Ib	14.02	13.51	OSC	0.041	0.020	M13	–	–
SN 2014C	Ib	16.04	14.93	OSC	0.078	0.670	M15	–	–
SN 2015ah	Ib	17.10	16.50	P19	0.071*	0.020	P19	0.09	2.00
SN 2015ap	Ib	15.71	15.20	P19	0.037*	0.000	P19	0.12	1.80
iPTF13bvn	Ib	15.91	15.21	OSC	0.028	0.044	P16	–	–
SN 1994I	Ic	13.83	12.87	OSC	0.031	0.300	P16	0.07	0.61
SN 2004aw	Ic	18.11	17.12	OSC	0.018	0.350	P16	0.23	4.90
SN 2004dn	Ic	18.69	17.32	OSC	0.041	0.520	D11	0.16	3.10
SN 2004fe	Ic	17.55	16.88	OSC	0.021	0.000	T18	0.16	1.92
SN 2004gt	Ic	16.36	15.40	S18	0.040	0.237	S18	0.16	3.75
SN 2005aw	Ic	17.24	15.99	OSC	0.053	0.496	S18	0.16	3.50
SN 2005mf	Ic	18.90	17.96	OSC	0.015	0.380	D11	0.26	2.19
SN 2007gr	Ic	13.48	12.88	OSC	0.053	0.030	P16	–	–
SN 2007hn	Ic	19.17	18.28	OSC	0.071	0.170	S18	0.21	1.65
SN 2011bm	Ic	17.11	16.52	OSC	0.029	0.032	P16	0.63	14.43
SN 2013F	Ic	19.15	17.13	P19	0.018*	1.400	P19	0.15	1.40
SN 2013ge	Ic	15.64	14.76	OSC	0.020	0.047	P16	–	–
SN 2014L	Ic	16.20	15.04	OSC	0.034	0.670	Z18	–	–
SN 2016iae	Ic	16.14	14.99	P19	0.014*	0.650	P19	0.13	2.20
SN 2016P	Ic	17.41	16.62	P19	0.024*	0.050	P19	0.09	1.50
SN 2017ein	Ic	16.01	15.26	V18	0.019*	0.340	V18	–	–
SN 2020oi	Ic	14.57	13.82	R20	0.023*	0.000	R20	0.07	0.71
LSQ14efd	Ic	19.79	18.96	OSC	0.032*	0.000	B17	0.25	2.49

Note. — The first five columns give the name, claimed SN type, $B-$band magnitude at the V-band peak, $V-$band magnitude at the peak, and the references from which photometric data were extracted. The sixth column gives $E(B-V)_{\rm MW}$ from the OSC. $E(B-V)_{\rm MW}$ values with an asterisk were extracted from the same reference as for $E(B-V)_{\rm Host}$. The seventh and eighth columns give $E(B-V)_{\rm Host}$ and their references. References are abbreviated as follows. D11: Drout et al. (2011), E11: Elmhamdi et al. (2011), O12: Oates et al. (2012), M13: Milisavljevic et al. (2013), M15: Milisavljevic et al. (2015), P16: Prentice et al. (2016), B17: Barbarino et al. (2017), S18: Stritzinger et al. (2018), T18: Taddia et al. (2018), V18: Van Dyk et al. (2018), Z18: Zhang et al. (2018), P19: Prentice et al. (2019), R20: Rho et al. (2020), J20: Jin et al. (2020) submitted to ApJ. $M_{\rm Ni}$ and $M_{\rm ej}$ are obtained from averaging over all the available values from Richardson et al. (2006); Drout et al. (2011); Cano (2013); Taddia et al. (2015); Prentice et al. (2016); Lyman et al. (2016); Taddia et al. (2018) except for SN 2020oi from R20, and LSQ14efd from J20.

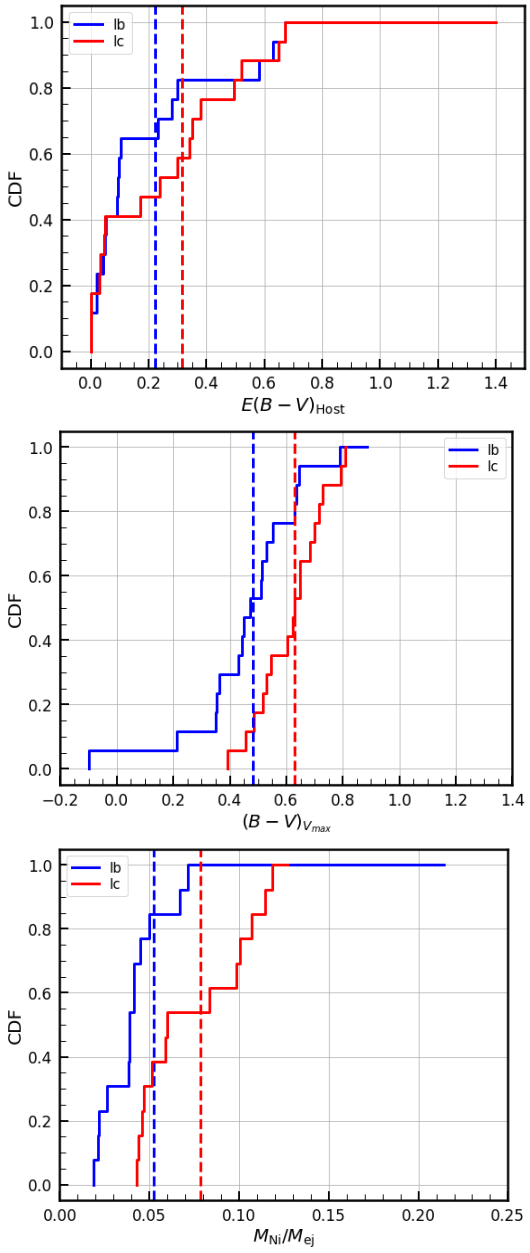

Figure 3.1 Cumulative distribution of $E(B-V)_{\rm Host}$ (top), $B-V$ color at V-band peak (middle), and $M_{\rm Ni}/M_{\rm ej}$ of SNe Ib/Ic (bottom). See the text for more details.

Jan. 1. 2000. and have photometric data more than 30 points were chosen from the OSC. We excluded superluminous SNe Ic, broad-lined SNe Ic, and Ca-rich SNe Ib to focus on the ordinary SNe Ib/Ic. Then SNe with a V-band light curve with a main peak are filtered, and then again with a criterion of having at least three B-band points and three V-band points within ± 5 days with respect to the V-band peak epoch for the purpose of obtaining a reasonably good color estimate at the V-band peak. Table 3.1 shows our SNe Ib/Ic sample.

The host galaxy extinction of stripped-envelope SNe is mostly non-negligible due to their dusty environments. We extract the host extinction $E(B-V)_{\rm Host}$ from the literature for each SN. A traditional way for determining the host extinction is to use the equivalent width of Na I D absorption lines (Poznanski et al. 2012). Another method is using a photometric property; the $V-R$ color at 10 days after the V-band peak, by taking advantage of its small scatter (Drout et al. 2011). Both methods are used in inferring $E(B-V)_{\rm Host}$ of SNe. See Table 3.1 for references for each SN for more details about the host extinction estimates. In the top panel of Figure 3.1, a cumulative distribution of $E(B-V)_{\rm Host}$ is presented for each SN type. The overall host extinction is larger for SNe Ic ($E(B-V)_{\rm Host}$=0.31) than for SNe Ib (0.22). This might imply different progenitor environments for SNe Ib and Ic. SNe Ic seem to originate from a more dusty environment, i.e., in which more active star formation is expected than SNe Ib.

Corrected for both the Milky Way extinction and the host galaxy extinction, the color of $B-V$ at the $V-$band peak, $(B-V)_{\rm Vmax}$ is obtained and presented in the middle panel of Figure 3.1. SNe Ib are systematically bluer than SNe Ic; SNe Ib have $(B-V)_{\rm Vmax}$=0.48, and SNe Ic have 0.63 on average, showing a color difference of $\Delta(B-V)_{\rm Vmax} \approx 0.15$. $M_{\rm Ni}$ and $M_{\rm ej}$ of the same set of SNe are extracted from the literature, and their ratios are calculated and presented in the bottom panel of Figure 3.1. SNe Ic have a systematically larger ^{56}Ni mass to ejecta mass ratio

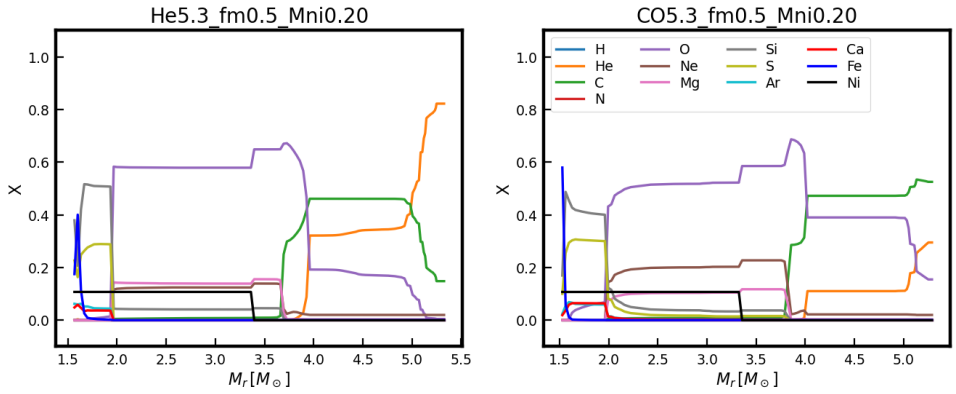

Figure 3.2 Chemical abundance profiles of the representative He star model and CO star model.

($M_{\rm Ni}/M_{\rm ej}$=0.08) than SNe Ib ($M_{\rm Ni}/M_{\rm ej}$=0.05).

3.3 Supernova models

We consider three possible explanations for the systematic difference of the optical color in SNe Ib/Ic: difference in the progenitor chemical structures, in degrees of ^{56}Ni mixing, and in the ^{56}Ni mass over the ejecta mass. We consider helium-rich and helium-poor progenitors of various $M_{\rm ej}$. Then we construct SN models with different degrees of ^{56}Ni mixing and different amounts of ^{56}Ni to explore the validity of each explanation.

3.3.1 Methods and physical assumptions

We consider various final masses of He stars (helium-rich progenitors which contain more than $0.6M_\odot$ of helium) and CO stars (helium-poor progenitors which contain less than $0.2M_\odot$ of helium) (See Table 3.2). The final masses span 3.1-5.7$M_\odot$, and the ejecta masses span 1.7-4.1$M_\odot$. The explored range of the ejecta mass encompasses most of the observed $M_{\rm ej}[M_\odot]$ values of $2.0-5.0$ of SNe Ib/Ic (Cano 2013; Lyman

Table 3.2 Model pre-SN properties

Name	$M_{\rm ej}$ $[M_\odot]$	R $[R_\odot]$	$M_{\rm CO}$ $[M_\odot]$	$Y_{\rm s}$	$m_{\rm He}$ $[M_\odot]$	$M_{\rm Fe}$ $[M_\odot]$	$M_{\rm ext}$ $[M_\odot]$
He3.1	1.73	31.66	1.56	0.98	1.43	1.30	0.018
He3.5	2.06	4.77	2.02	0.98	1.44	1.41	0.022
He3.9	2.40	6.73	2.17	0.98	1.66	1.44	0.024
He4.2	2.76	2.45	2.63	0.98	1.58	1.45	0.027
He5.3	3.75	0.87	3.95	0.82	0.63	1.50	0.038
He5.6	4.10	1.62	3.64	0.98	1.62	1.48	0.041
CO3.2	1.77	0.20	3.18	0.12	0.04	1.39	0.018
CO3.6	2.05	0.21	3.61	0.12	0.07	1.53	0.021
CO3.9	2.49	0.77	3.92	0.49	0.10	1.41	0.024
CO4.2	2.72	0.22	4.19	0.08	0.06	1.45	0.027
CO5.3	3.76	0.59	5.13	0.30	0.22	1.46	0.038
CO5.7	4.08	0.20	5.56	0.30	0.17	1.63	0.041

Note. — $M_{\rm ej}$: ejecta mass; R: progenitor radius; $M_{\rm CO}$: He-deficient core mass which has helium mass fraction lower than 0.2; $Y_{\rm s}$: surface helium mass fraction; $m_{\rm He}$: total helium mass; $M_{\rm Fe}$: iron core mass; $M_{\rm ext}$: CSM mass

et al. 2016; Taddia et al. 2018). Progenitor models are named to indicate whether it is He star or CO star and its total mass: He3.1 refers to a He star progenitor with its total mass of $3.1M_{\odot}$. We will use the same notation to refer to the SN model from the respective progenitor model. Refer to the Table 3.2 for more details.

SN models are calculated by using four different ^{56}Ni masses and two kinetic energies. Since the explosive nucleosynthesis is not implemented in the current version of STELLA, ^{56}Ni is artificially introduced with its masses being $0.07M_{\odot}$, $0.14M_{\odot}$, $0.20M_{\odot}$, and $0.25M_{\odot}$. Kinetic energies of 1B and 2B are obtained by controlling the explosion energy. Again, this set of the ^{56}Ni mass and the kinetic energy can cover most of the observed SNe Ib/Ic (Taddia et al. 2018). The distribution of ^{56}Ni is set to follow a step-function with its non-zero part spanning $f_{\rm m}$ of its ejecta, and the mass cut is set to correspond to the surface of the iron core, i.e., $X_{\rm Ni}(M_r) = \frac{M_{\rm Ni}}{f_{\rm m}(M_{\rm tot}-M_{\rm cut})}$ for $M_{\rm cut} < M_r < f_{\rm m}(M_{\rm tot} - M_{\rm cut}) + M_{\rm cut}$ and $X_{\rm Ni}(M_r) = 0$ elsewhere. Here, M_r is the mass coordinate, $M_{\rm cut}$ is the mass cut, $M_{\rm tot}$ is the total mass of the progenitor, and $f_{\rm m}$ is the ^{56}Ni distribution parameter; $f_{\rm m}$=0.15, 0.5, and 1.0 are considered in the study. $f_{\rm m}$=0.15 might correspond to a SN in which weak ^{56}Ni mixing had occurred, $f_{\rm m}$=0.5 to moderate mixing, and $f_{\rm m}$=1.0 to strong mixing (^{56}Ni fully-mixed). The progenitor models are attached with CSM with a mass of 1% of their ejecta masses and an extent of 10^{14}cm to avoid relativistic effects which cannot be handled in the current version of STELLA.

STELLA is a one-dimensional multi-group radiative-hydrodynamics code for calculating SN light curves in multi-bands. SN explosion is treated as a thermal bomb at the mass cut, right above the iron core, and the code solves time-dependent radiative transfer equations and hydrodynamics equations simultaneously for 100 wavelengths bins. For more detailed information, see Blinnikov & Tolstov (2011). (Table for pre-supernova models and explosion properties)

3.3.2 Model color distribution

Both unweighted and weighted cumulative distribution functions of $(B-V)_{\rm Vmax}$ of our SN models are compared with the observation in Figure 3.3. To construct the weighted cumulative distribution function in the lower panel, we derive the distributions of $M_{\rm ej}$, $M_{\rm Ni}$, and $E_{\rm k}$ from the literature (Richardson et al. 2006; Drout et al. 2011; Cano 2013; Taddia et al. 2015; Prentice et al. 2016; Lyman et al. 2016; Taddia et al. 2018) and assigned weights to each model parameter. The assigned weights are ($M_{\rm ej}[M_\odot]$, weight; w): (1.7-1.8, 0.19), (2.0-2.1, 0.20), (2.4-2.5, 0.19), (2.7-2.8, 0.19), (3.7-3.8, 0.12), (4.0-4.1, 0.10), ($M_{\rm Ni}[M_\odot]$, w): (0.07, 0.20), (0.14, 0.33), (0.20, 0.29), (0.25, 0.19), and ($E_{\rm k}$[B], w): (1, 0.68), (2, 0.32). In both unweighted and weighted cases, He star models show bluer color of $(B-V)_{\rm Vmax} = 0.35-0.43$, than CO star models of $(B-V)_{\rm Vmax} = 0.55-0.61$ except for the fully mixed case, $f_{\rm m}$=1.0. The systematic color difference yield $\Delta(B-V)_{\rm Vmax} = 0.15-0.25$, which is comparable to the observed color gap between SNe Ib/Ic. Although using different sets of weights results in different cumulative distribution functions, qualitative features do not change.

3.4 Color difference

3.4.1 Chemical structure of the progenitor

The systematic color difference between He star and CO star models in Figure 3.3 indicates that the chemical structure difference in progenitors affects optical color at the V-band peak.

Figure 3.4 presents the Rosseland-mean opacity and temperature evolution in the ejecta. The Rosseland-mean opacity, κ[g/cm^2], is below 0.02 in He4.2 model at $M_r[M_\odot] \gtrsim 3.8$ at $5-28$ d while it is in between $\kappa = 0.02-0.06$ in CO4.2 model. Thus the photosphere retreats inwardly faster in He4.2 model than in CO4.2 model;

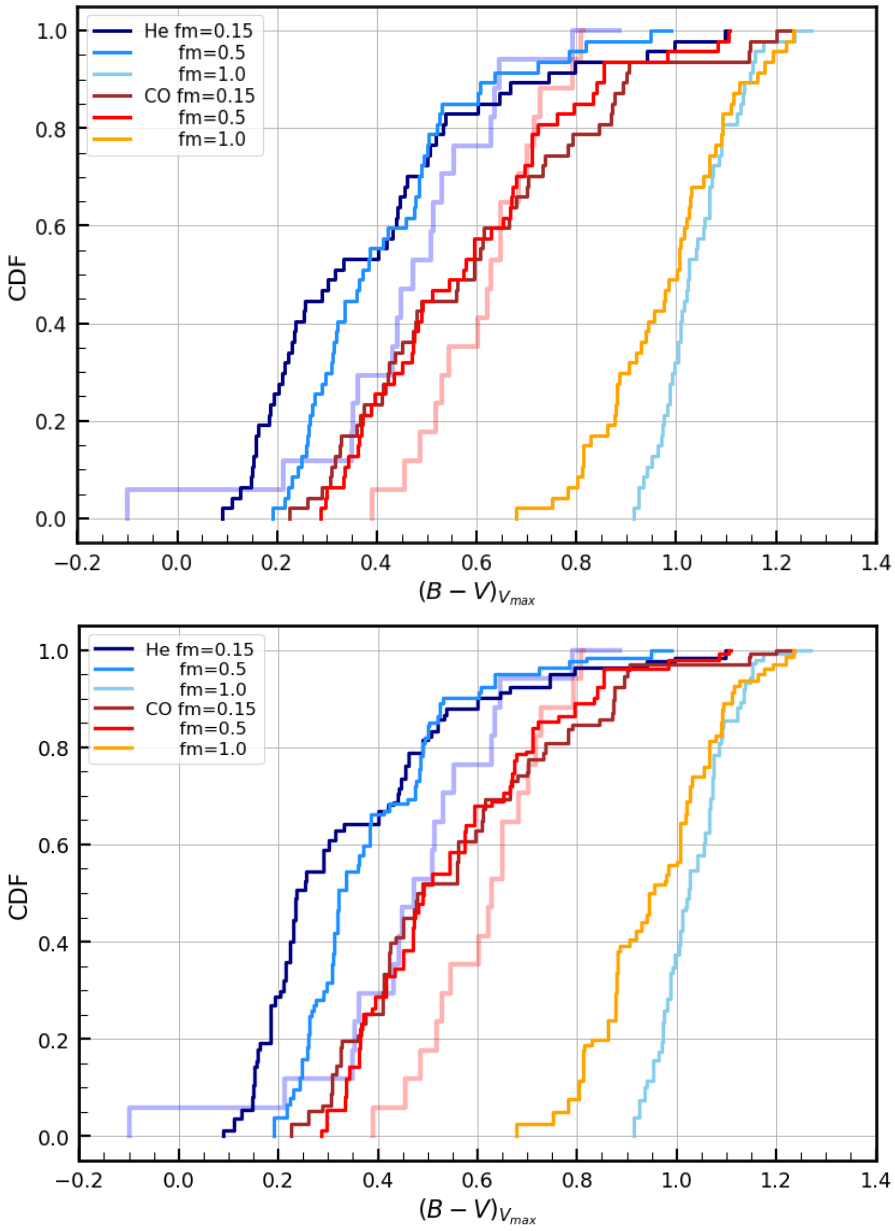

Figure 3.3 Cumulative distribution of $(B-V)_{\rm Vmax}$ of He star models and CO star models of different $f_{\rm m}$. Upper panel corresponds to the unweighted distribution, lower panel corresponds to the weighted distribution as described in Section 3.3.2. Observed SNe are overlapped as blue (SNe Ib) and red (SNe Ic) semitransparent lines. Average values in the unweighted distribution are $(B-V)_{\rm Vmax}$=0.40 (He $f_{\rm m}$=0.15), 0.43 (He $f_{\rm m}$=0.50), 1.04 (He $f_{\rm m}$=1.0), 0.61 (CO $f_{\rm m}$=0.15), 0.59 (CO $f_{\rm m}$=0.5), and 0.99 (CO $f_{\rm m}$=1.0). Average values in the weighted distribution are $(B-V)_{\rm Vmax}$=0.35 (He $f_{\rm m}$=0.15), 0.39 (He $f_{\rm m}$=0.50), 1.03 (He $f_{\rm m}$=1.0), 0.56 (CO $f_{\rm m}$=0.15), 0.55 (CO $f_{\rm m}$=0.5), and 0.96 (CO $f_{\rm m}$=1.0).

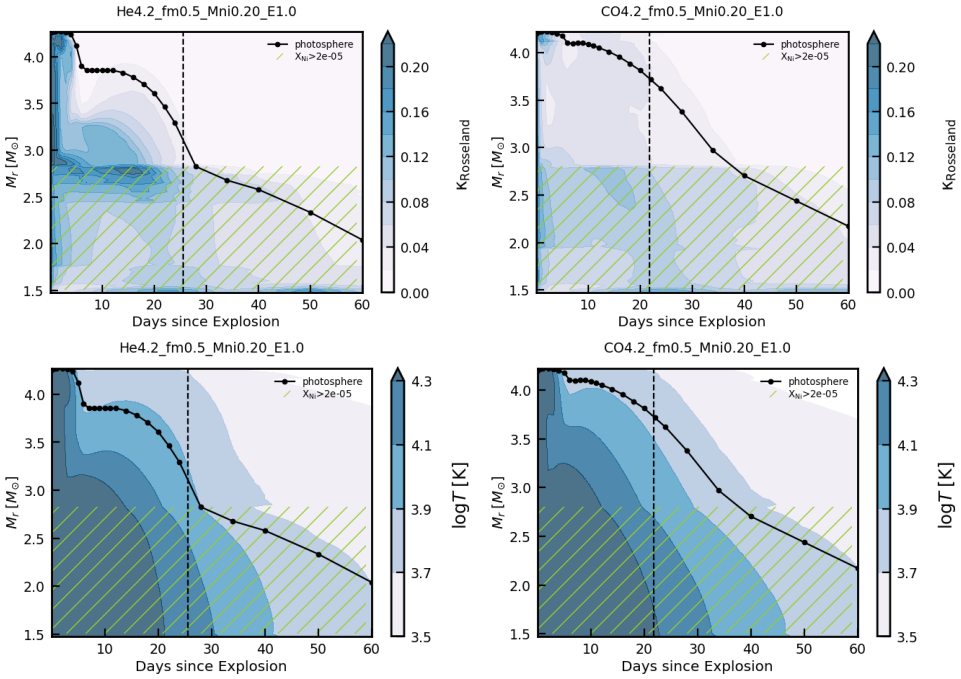

Figure 3.4 The Rosseland-mean opacity evolution and the temperature evolution of a representative He4.2 model and a CO4.2 model. Vertical dashed line represents the epoch of $V-$band peak.

starting from the outermost layer of $M_r[M_\odot] \approx 4.2$ in both models, the photosphere is located at $M_r[M_\odot] = 3.9$ at 6 d and $M_r[M_\odot] = 2.8$ at 28 d in He4.2 model while it is located at $M_r[M_\odot] = 4.1$ and $M_r[M_\odot] = 3.4$ at the same epochs in CO4.2 model. The photosphere located at deeper layers allows hotter photons to escape from the inner ^{56}Ni-heated region. The photospheric temperature at $5-28$ d is hotter in He4.2 model ($3.9 < \log T[\mathrm{K}] < 4.1$) than in CO4.2 model ($3.7 < \log T[\mathrm{K}] < 3.9$). This makes the spectral energy distribution harder and the optical color bluer ($(B-V)$ smaller) at the V-band peak in He4.2 model than in CO4.2 model.

The result implies that chemical structures in progenitors contribute significantly to the optical color at the V-band peak. Helium-rich progenitors lead to bluer color than helium-poor stars, which is in agreement with the notion that SNe Ib stem from helium-rich progenitors and SNe Ic from helium-poor progenitors.

3.4.2 ^{56}Ni mixing

A strong outward ^{56}Ni mixing can yield redder color at V-band peak. In Figure 3.3, fully mixed cases (f_m=1.0) show much redder color as $(B-V)_\mathrm{Vmax} \approx 1.0$ than weakly/moderately mixed cases (f_m=0.15, 0.5) of $(B-V)_\mathrm{Vmax} \approx 0.4-0.6$. Figure 3.5 shows the Rosseland-mean opacity and temperature evolution of models with different f_m. Compared to f_m=1.0, the photosphere in f_m=0.15 retreats faster and stays in the hot ^{56}Ni-heated region ($\log T[\mathrm{K}] > 3.9$ at 11 - 30 d) during which the V-band peak appears at 26 d. On the other hand, the photosphere in f_m=1.0 recedes inwardly more slowly and monotonically cools down ($\log T[\mathrm{K}] < 3.9$ after 21 d) until the V-band peak appears at 22 d.

It was shown that progenitors of SNe Ic require stronger mixing to explain the observed monotonic redward evolution while those of SNe Ib require weak/moderate mixing to explain the early-time blueward evolution (Yoon et al. 2019). This poses that the combined effects of different abundance structures and different degrees of

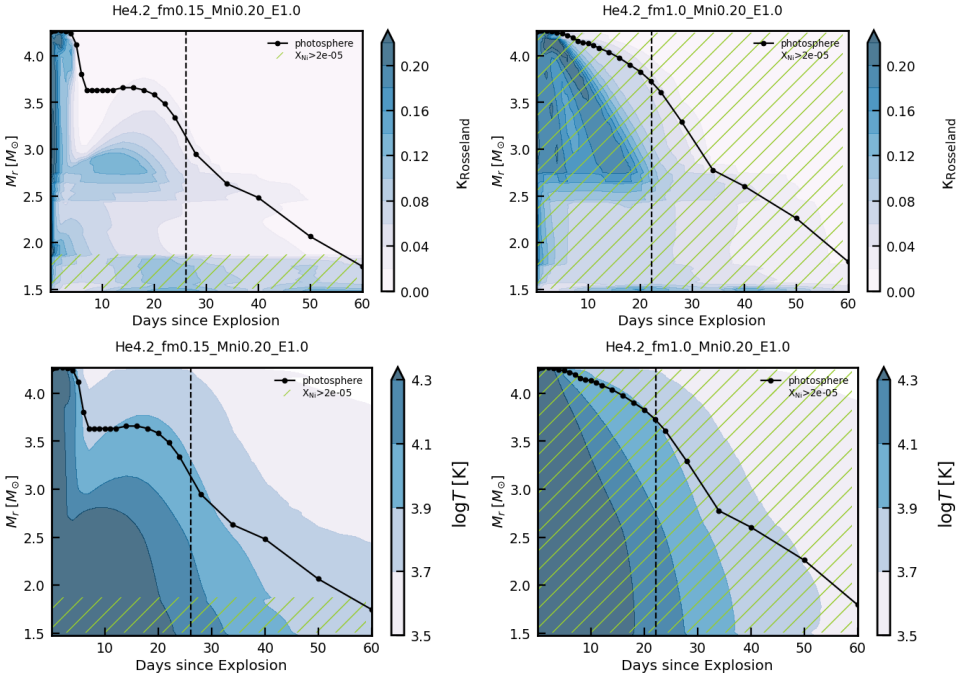

Figure 3.5 The Rosseland-mean opacity evolution and the temperature evolution of models with different degrees of ^{56}Ni mixing. Left panels correspond to $f_{\rm m}$=0.15, right panels correspond to $f_{\rm m}$=1.0. Vertical dashed line represents the epoch of $V-$band peak.

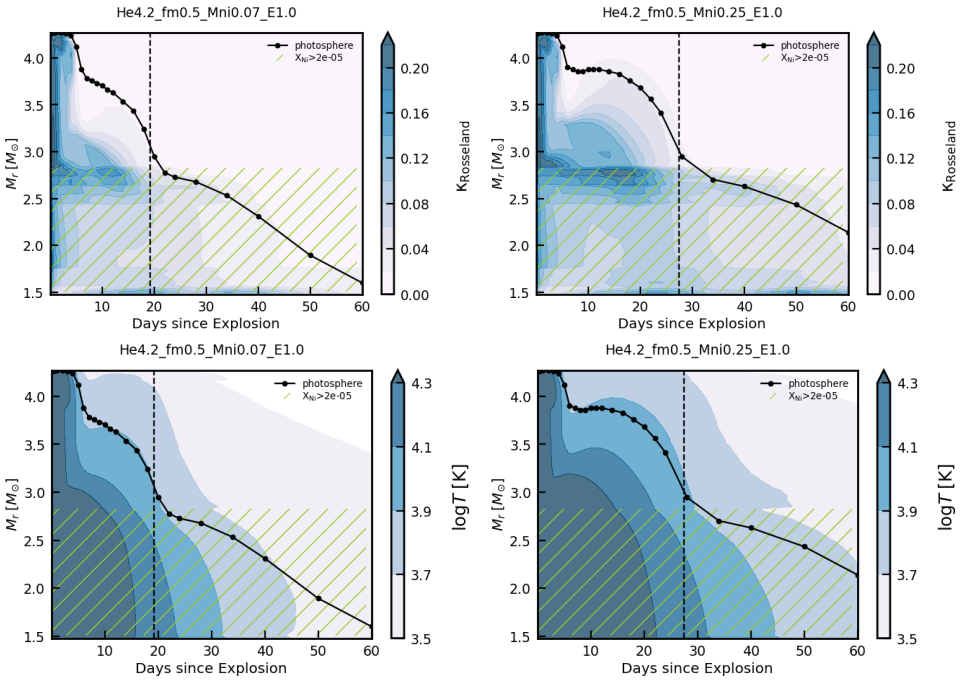

Figure 3.6 The Rosseland-mean opacity evolution and the temperature evolution of models with different ^{56}Ni mass. Left panels correspond to $M_{\rm Ni}$=0.07$M_\odot$, right panels correspond to $M_{\rm Ni}$=0.25$M_\odot$. Vertical dashed line represents the epoch of $V-$band peak.

^{56}Ni mixing play a role in the SNe Ib/Ic color difference. A stronger mixing in a helium-rich progenitor alone is not likely to be responsible for the red color of SNe Ic since this condition favors the formation of He I lines in helium-rich progenitors.

3.4.3 ^{56}Ni mass over ejecta mass

SN ejecta with more ^{56}Ni has a larger thermal energy due to the extra heating. Figure 3.6 compares the Rosseland-mean opacity and the temperature evolution for different $M_{\rm Ni}$ masses. In the model with $M_{\rm Ni}$=0.25$M_\odot$, the ejecta is hotter at every mass zone for a given epoch compared to the model with $M_{\rm Ni}$=0.07$M_\odot$. The

photosphere of the model with $M_{\rm Ni}$=0.25$M_{\odot}$ retreats more slowly than that of $M_{\rm Ni}$=0.07$M_{\odot}$ does, and its temperature remains in between $\log T[{\rm K}] = 3.9 - 4.1$ at $8 - 29$ d. The V-band peak occurs at 27 d. The photospheric temperature of the smaller $M_{\rm Ni}$ stays in the same range at $11 - 19$ d. The V-band peak is reached at 19 d when the photospheric temperature traverses $\log T[{\rm K}] = 3.9$ downward. This comparison illustrates that a larger $M_{\rm Ni}$ leads to bluer optical color at the V-band peak, for a given ejecta mass. In Figure 3.3, the models with a small (large) $M_{\rm Ni}$ comprises the red (blue) end of the color distribution.

If $M_{\rm Ni}/M_{\rm ej}$ was systematically larger in SNe Ib than SNe Ic, this might have led to bluer color. On the contrary, SNe Ic have larger $M_{\rm Ni}/M_{\rm ej}$ compared to SNe Ib as can be seen in Figure 3.1 at least for our SNe sample. Thus this implies that the optical color difference is not due to larger $M_{\rm Ni}/M_{\rm ej}$ in SNe Ib than in SNe Ic.

3.5 Conclusions

We show that the optical colors of SNe Ib and Ic are systematically different at the V-band peak and argue that progenitors with distinctive chemical structures can explain the color gap. SNe Ib and Ic have average values of $(B-V)_{\rm Vmax} = 0.48$ and 0.63, respectively, showing ~ 0.15 of difference (Section 3.2). SN models from helium-rich progenitors (He star models) yield bluer color than those from helium-poor progenitors (CO star models) as long as ^{56}Ni mixing is not extreme; He star models have $(B-V)_{\rm Vmax}$=0.35 − 0.40, and CO star models have 0.55 − 0.60, showing a comparable color difference of $\sim 0.15 - 0.25$ to the observation (Section 3.3). Given that SNe Ib color evolution is well-explained by weak/moderate ^{56}Ni mixing and SNe Ic by strong mixing (Yoon et al. 2019), it is likely that the chemical structure difference in progenitors as well as different degrees of mixing play a key role in bluer/redder color of SNe Ib/Ic (Section 3.4). Inhomogeneity seems to exist in $M_{\rm Ni}/M_{\rm ej}$ of SNe Ib/Ic, but it does not serve to make the color gap of our

concern since larger $M_{\rm Ni}/M_{\rm ej}$ in SNe Ic would make the color bluer as opposed to the observation.

The results provide further evidence rebutting the existence of hidden helium in SNe Ic. This is in line with recent spectroscopic studies on the hidden helium problem (Teffs et al. 2020; Williamson et al. 2020; Dessart et al. 2020), none of which support massive helium content in SNe Ic progenitors. With regard to stellar evolution, a recent study by Yoon et al. (2017) predicts that Wolf-Rayet stars at the pre-SN stage would have a dichotomy in helium mas and surface helium mass fraction, supporting a distinctively different properties of SNe Ib/Ic progenitors.

This study is subject to a few limitations. First of all, the code used in the study might not predict color correctly due to some physical simplifications implemented in the code, e.g., LTE assumption for level distributions, limited number of spectral lines, lack of fluorescence effect and etc. Detailed spectrum calculation along with photometry is required for more rigorous qualitative comparison with the observation. Secondly, only a limited number of SNe Ib/Ic samples ($\sim$20 for each subtype) are used for the analysis due to the lack of either photometric data or extinction data. Future acquisition of large samples of SNe Ib/Ic will help to confirm the results and may shed a light on the evolution of massive stars.

Chapter 4

Concluding Remarks

In this thesis, the physical properties of Type Ib and Type Ic supernovae (SNe Ib/Ic) progenitors are explored by using numerical simulations. The light curves and color of SNe are photometric indicators that enable us to infer the progenitor natures after the explosions. By comparing the observed SNe Ib/Ic light curves and color with models, we examine circumstellar matter (CSM) structure of unusual SNe Ic progenitors and different progenitor properties of SNe Ib and Ic, both of which have not been discussed in depth before.

In the first study (Chapter 2), we investigate three double-peaked SNe Ic (LSQ14efd, iPTF15dtg, and SN 2020bvc) which showed bright post-breakout emission in the optical bands by considering CSM interaction. The light curves and color during the interaction-powered phase (IPP) vary according to the CSM structure; SN models with more massive or larger CSM have brighter IPP peaks, more extended IPP duration, and bluer color during the IPP within our grid. Through comparison, we find models that are consistent with each SN data, all of which require CSM mass of $M_{\rm CSM} \approx 0.1 M_\odot$ and radius of $R_{\rm CSM} = 10^{13} - 10^{14}$ cm. This CSM structure corresponds to an extreme mass-loss rate of $\dot{M} \gtrsim 1.0\ M_\odot\ {\rm yr}^{-1}\ (v_{\rm w}/200\ {\rm km/s})$ within about one year before the SN explosion.

In the second study (Chapter 3), it is shown that SNe Ib and Ic show systematically different $B-V$ color at the V-band peak: $(B-V)_{\rm Vmax} = 0.48$ (SNe Ib) and 0.63 (SNe Ic), on average. We consider three different scenarios to explain the systematic color difference. Firstly, progenitors with different chemical structures can make the color different; helium-rich (helium-poor) progenitors result in bluer (redder) color. Secondly, different degrees of ^{56}Ni mixing can affect the color; SN models with fully mixed ^{56}Ni have redder color than those with weakly/moderately mixed ^{56}Ni. Thirdly, different ratios of the ^{56}Ni mass to the ejecta mass can matter; a larger $M_{\rm Ni}/M_{\rm ej}$ make color bluer. Our analysis suggests that progenitors with different chemical structures (SNe Ib from helium-rich progenitors and SNe Ic from helium-poor progenitors) along with different degrees of ^{56}Ni mixing (SNe Ic with stronger mixing than SNe Ib) be the most plausible scenario.

SNe provide a posteriori clues of the stellar evolution prior to the explosions. Especially, SNe Ib/Ic originate from massive stars of which their hydrogen envelopes are stripped off. Either stellar wind or binary interaction is a possible mass-loss channel, but the detailed nature of mass-loss mechanism is still in debate. The research conducted in this work provide evidence for distinctively different natures of SNe Ib and Ic, i.e., considerably different mass-loss rates and/or evolutionary histories between the two SN subtypes. Also, the possibility of extreme mass-loss from some SNe Ic progenitors is implied in our study. Future works should explore extensive mass-loss channels for SNe Ib/Ic progenitors which can account for the dichotomy of SNe Ib and Ic and extreme mass-loss from some SN Ic progenitors.

Bibliography

Aguilera-Dena, D. R., Langer, N., Moriya, T. J., et al. 2018, ApJ, 858, 115. doi:10.3847/1538-4357/aabfc1

Anderson, J. P. 2019, A&A, 628, A7. doi:10.1051/0004-6361/201935027

Arnett, W. D. 1982, ApJ, 253, 785. doi:10.1086/159681

Barbarino, C., Botticella, M. T., Dall'Ora, M., et al. 2017, MNRAS, 471, 2463. doi:10.1093/mnras/stx1709

Barbarino, C., Sollerman, J., Taddia, F., et al. 2020, arXiv:2010.08392

Bersten, M. C., Tanaka, M., Tominaga, N., et al. 2013, ApJ, 767, 143. doi:10.1088/0004-637X/767/2/143

Blinnikov, S. I., Eastman, R., Bartunov, O. S., et al. 1998, ApJ, 496, 454. doi:10.1086/305375

Blinnikov, S., Lundqvist, P., Bartunov, O., et al. 2000, ApJ, 532, 1132. doi:10.1086/308588

Blinnikov, S. I., Röpke, F. K., Sorokina, E. I., et al. 2006, A&A, 453, 229. doi:10.1051/0004-6361:20054594

Blinnikov, S. I. & Tolstov, A. G. 2011, Astronomy Letters, 37, 194. doi:10.1134/S1063773711010051

Blinnikov, S. 2017, Handbook of Supernovae, 843. doi:10.1007/978-3-319-21846-5_31

Cano, Z. 2013, MNRAS, 434, 1098. doi:10.1093/mnras/stt1048

Dessart, L., Hillier, D. J., Livne, E., et al. 2011, MNRAS, 414, 2985. doi:10.1111/j.1365-2966.2011.18598.x

Dessart, L., Hillier, D. J., Li, C., et al. 2012, MNRAS, 424, 2139. doi:10.1111/j.1365-2966.2012.21374.x

Dessart, L., Hillier, D. J., Woosley, S., et al. 2015, MNRAS, 453, 2189. doi:10.1093/mnras/stv1747

Dessart, L., Hillier, D. J., & Wilk, K. D. 2018, A&A, 619, A30. doi:10.1051/0004-6361/201833278

Dessart, L., Yoon, S.-C., Livne, E., et al. 2018, A&A, 612, A61. doi:10.1051/0004-6361/201732363

Dessart, L., Yoon, S.-C., Aguilera-Dena, D. R., et al. 2020, A&A, 642, A106. doi:10.1051/0004-6361/202038763

Drout, M. R., Soderberg, A. M., Gal-Yam, A., et al. 2011, ApJ, 741, 97. doi:10.1088/0004-637X/741/2/97

Elmhamdi, A., Tsvetkov, D., Danziger, I. J., et al. 2011, ApJ, 731, 129. doi:10.1088/0004-637X/731/2/129

Ergon, M., Jerkstrand, A., Sollerman, J., et al. 2015, A&A, 580, A142. doi:10.1051/0004-6361/201424592

Förster, F., Moriya, T. J., Maureira, J. C., et al. 2018, Nature Astronomy, 2, 808. doi:10.1038/s41550-018-0563-4

Folatelli, G., Contreras, C., Phillips, M. M., et al. 2006, ApJ, 641, 1039. doi:10.1086/500531

Fuller, J. 2017, MNRAS, 470, 1642. doi:10.1093/mnras/stx1314

Fuller, J. & Ro, S. 2018, MNRAS, 476, 1853. doi:10.1093/mnras/sty369

González-Gaitán, S., Tominaga, N., Molina, J., et al. 2015, MNRAS, 451, 2212. doi:10.1093/mnras/stv1097

Grasberg, E. K. 1981, Soviet Ast., 25, 85

Guillochon, J., Parrent, J., Kelley, L. Z., et al. 2017, ApJ, 835, 64. doi:10.3847/1538-4357/835/1/64

Hachinger, S., Mazzali, P. A., Taubenberger, S., et al. 2012, MNRAS, 422, 70. doi:10.1111/j.1365-2966.2012.20464.x

Ho, A. Y. Q., Kulkarni, S. R., Perley, D. A., et al. 2020, ApJ, 902, 86. doi:10.3847/1538-4357/aba630

Kasen, D. 2010, ApJ, 708, 1025. doi:10.1088/0004-637X/708/2/1025

Kasen, D., Metzger, B. D., & Bildsten, L. 2016, ApJ, 821, 36. doi:10.3847/0004-637X/821/1/36

Khazov, D., Yaron, O., Gal-Yam, A., et al. 2016, ApJ, 818, 3. doi:10.3847/0004-637X/818/1/3

Kozyreva, A., Shingles, L., Mironov, A., et al. 2020, MNRAS, 499, 4312. doi:10.1093/mnras/staa2704

Liu, Y.-Q., Modjaz, M., Bianco, F. B., et al. 2016, ApJ, 827, 90. doi:10.3847/0004-637X/827/2/90

Lucy, L. B. 1991, ApJ, 383, 308. doi:10.1086/170787

Lyman, J. D., Bersier, D., James, P. A., et al. 2016, MNRAS, 457, 328. doi:10.1093/mnras/stv2983

Milisavljevic, D., Soderberg, A. M., Margutti, R., et al. 2013, ApJ, 770, L38. doi:10.1088/2041-8205/770/2/L38

Milisavljevic, D., Margutti, R., Kamble, A., et al. 2015, ApJ, 815, 120. doi:10.1088/0004-637X/815/2/120

Modjaz, M., Stanek, K. Z., Garnavich, P. M., et al. 2006, ApJ, 645, L21. doi:10.1086/505906

Moriya, T., Tominaga, N., Blinnikov, S. I., et al. 2011, MNRAS, 415, 199. doi:10.1111/j.1365-2966.2011.18689.x

Moriya, T. J., Yoon, S.-C., Gräfener, G., et al. 2017, MNRAS, 469, L108. doi:10.1093/mnrasl/slx056

Moriya, T. J., Sorokina, E. I., & Chevalier, R. A. 2018, Space Sci. Rev., 214, 59. doi:10.1007/s11214-018-0493-6

Moriya, T. J., Förster, F., Yoon, S.-C., et al. 2018, MNRAS, 476, 2840. doi:10.1093/mnras/sty475

Moriya, T. J., Suzuki, A., Takiwaki, T., et al. 2020, MNRAS, 497, 1619. doi:10.1093/mnras/staa2060

Morozova, V., Piro, A. L., & Valenti, S. 2018, ApJ, 858, 15. doi:10.3847/1538-4357/aab9a6

Nadezhin, D. K. & Frank-Kamenetskii, D. A. 1965, Soviet Ast., 8, 674

Nicholl, M., Smartt, S. J., Jerkstrand, A., et al. 2015, ApJ, 807, L18. doi:10.1088/2041-8205/807/1/L18

Nicholl, M. & Smartt, S. J. 2016, MNRAS, 457, L79. doi:10.1093/mnrasl/slv210

Nugis, T. & Lamers, H. J. G. L. M. 2000, A&A, 360, 227

Oates, S. R., Bayless, A. J., Stritzinger, M. D., et al. 2012, MNRAS, 424, 1297. doi:10.1111/j.1365-2966.2012.21311.x

Panov, I. V., Glazyrin, S. I., Röpke, F. K., et al. 2018, Astronomy Letters, 44, 309. doi:10.1134/S1063773718050031

Paxton, B., Bildsten, L., Dotter, A., et al. 2011, ApJS, 192, 3. doi:10.1088/0067-0049/192/1/3

Paxton, B., Cantiello, M., Arras, P., et al. 2013, ApJS, 208, 4. doi:10.1088/0067-0049/208/1/4

Paxton, B., Marchant, P., Schwab, J., et al. 2015, ApJS, 220, 15. doi:10.1088/0067-0049/220/1/15

Paxton, B., Schwab, J., Bauer, E. B., et al. 2018, ApJS, 234, 34. doi:10.3847/1538-4365/aaa5a8

Phillips, M. M. 1993, ApJ, 413, L105. doi:10.1086/186970

Piro, A. L. & Nakar, E. 2013, ApJ, 769, 67. doi:10.1088/0004-637X/769/1/67

Potashov, M. S., Blinnikov, S. I., & Utrobin, V. P. 2017, Astronomy Letters, 43, 36. doi:10.1134/S1063773717010030

Poznanski, D., Prochaska, J. X., & Bloom, J. S. 2012, MNRAS, 426, 1465. doi:10.1111/j.1365-2966.2012.21796.x

Prentice, S. J., Mazzali, P. A., Pian, E., et al. 2016, MNRAS, 458, 2973. doi:10.1093/mnras/stw299

Prentice, S. J., Ashall, C., James, P. A., et al. 2019, MNRAS, 485, 1559. doi:10.1093/mnras/sty3399

Quataert, E. & Shiode, J. 2012, MNRAS, 423, L92. doi:10.1111/j.1745-3933.2012.01264.x

Rho, J., Evans, A., Geballe, T. R., et al. 2020, arXiv:2010.00662

Richardson, D., Branch, D., & Baron, E. 2006, AJ, 131, 2233. doi:10.1086/500578

Smith, N. 2014, ARA&A, 52, 487. doi:10.1146/annurev-astro-081913-040025

Smith, N. 2017, Handbook of Supernovae, 403. doi:10.1007/978-3-319-21846-5_38

Stritzinger, M. D., Taddia, F., Burns, C. R., et al. 2018, A&A, 609, A135. doi:10.1051/0004-6361/201730843

Taddia, F., Sollerman, J., Leloudas, G., et al. 2015, A&A, 574, A60. doi:10.1051/0004-6361/201423915

Taddia, F., Fremling, C., Sollerman, J., et al. 2016, A&A, 592, A89. doi:10.1051/0004-6361/201628703

Taddia, F., Stritzinger, M. D., Bersten, M., et al. 2018, A&A, 609, A136. doi:10.1051/0004-6361/201730844

Taddia, F., Sollerman, J., Fremling, C., et al. 2019, A&A, 621, A64. doi:10.1051/0004-6361/201833688

Teffs, J., Ertl, T., Mazzali, P., et al. 2020, MNRAS, 499, 730. doi:10.1093/mnras/staa2549

Van Dyk, S. D., Zheng, W., Brink, T. G., et al. 2018, ApJ, 860, 90. doi:10.3847/1538-4357/aac32c

Wellons, S., Soderberg, A. M., & Chevalier, R. A. 2012, ApJ, 752, 17. doi:10.1088/0004-637X/752/1/17

Williamson, M., Kerzendorf, W., & Modjaz, M. 2020, arXiv:2010.10528

Woosley, S. E. & Heger, A. 2015, ApJ, 810, 34. doi:10.1088/0004-637X/810/1/34

Woosley, S. E. 2017, ApJ, 836, 244. doi:10.3847/1538-4357/836/2/244

Woosley, S. E. 2019, ApJ, 878, 49. doi:10.3847/1538-4357/ab1b41

Yoon, S.-C. & Cantiello, M. 2010, ApJ, 717, L62. doi:10.1088/2041-8205/717/1/L62

Yoon, S.-C., Woosley, S. E., & Langer, N. 2010, ApJ, 725, 940. doi:10.1088/0004-637X/725/1/940

Yoon, S.-C. 2015, PASA, 32, e015. doi:10.1017/pasa.2015.16

Yoon, S.-C., Dessart, L., & Clocchiatti, A. 2017, ApJ, 840, 10. doi:10.3847/1538-4357/aa6afe

Yoon, S.-C., Chun, W., Tolstov, A., et al. 2019, ApJ, 872, 174. doi:10.3847/1538-4357/ab0020

Zhang, J., Wang, X., Vinkó, J., et al. 2018, ApJ, 863, 109. doi:10.3847/1538-4357/aaceaf

Appendix A

Appendix for Chapter 2

Table A.1 IPP properties of 4P models for LSQ14efd with $f_{\rm m}$= 0.15

$E_{\rm burst}$ [B]	$M_{\rm CSM}$ [$M_\odot$]	log$R_{\rm CSM}$ [cm]	$M_{V,\rm peak}$ [mag]	$t_{\rm rise}$ [d]	$\Delta t_{0.3}$ [d]	$s_{3\sim10\rm d}$ [mag/d]
1	0.05	13	-15.79	2.35	1.75	0.29
		14	-16.26	2.89	2.76	0.21
		15	-17.23	4.05	3.46	0.08
	0.15	13	-16.26	3.88	2.84	0.32
		14	-16.79	5.39	4.79	0.08
		15	-17.82	6.71	6.18	0.04
	0.3	13	-16.55	5.71	3.66	0.16
		14	-17.16	7.93	6.36	0.04
		15	-18.09	9.19	9.15	0.01
1.5	0.05	13	-16.17	1.79	1.55	0.2
		14	-16.59	2.13	3.2	0.21
		15	-17.7	3.59	2.33	0.14
	0.15	13	-16.66	3.42	2.67	0.28
		14	-17.18	4.92	4.63	0.1
		15	-18.19	5.85	4.08	0.04
	0.3	13	-16.95	4.92	3.4	0.19
		14	-17.57	6.68	5.4	0.05
		15	-18.42	7.87	6.47	0.02
2	0.05	13	-16.39	1.61	1.49	0.15
		14	-16.83	1.88	3.18	0.21
		15	-17.92	3.14	2.49	0.16
	0.15	13	-16.92	2.97	2.53	0.26
		14	-17.45	4.14	4.29	0.11
		15	-18.42	5.4	3.51	0.05
	0.3	13	-17.16	4.44	3.52	0.19
		14	-17.87	6.16	4.91	0.06
		15	-18.62	7.32	6.35	0.02

Note. — $E_{\rm burst}$: explosion energy; $M_{\rm CSM}$: mass of the CSM; log$R_{\rm CSM}$: radius of the CSM; $M_{V,\rm peak}$: V-band maximum magnitude during the IPP; $t_{\rm rise}$: time from the explosion to the V-band maximum during the IPP, $\Delta t_{+0.3}$: time span between two 76% V-mag maximum (+0.3 mag) points during the IPP, one during its rise to the maximum and the other during its decline from the maximum; $s_{3\sim10\rm d}$: $B-V$ color evolution slope at 3∼10 day.

Table A.2 IPP properties of 8P models for LSQ14efd with $f_{\rm m}$= 0.15

$E_{\rm burst}$ [B]	$M_{\rm CSM}$ [$M_\odot$]	log$R_{\rm CSM}$ [cm]	$M_{V,\rm peak}$ [mag]	$t_{\rm rise}$ [d]	$\Delta t_{0.3}$ [d]	$s_{3\sim10\rm d}$ [mag/d]
5	0.05	13	-16.53	1.42	1.35	0.38
		14	-17.06	1.67	2.89	0.4
		15	-18.26	2.82	1.85	0.31
	0.15	13	-17.1	2.66	2.06	0.45
		14	-17.68	3.57	3.26	0.17
		15	-18.73	4.78	2.38	0.07
	0.3	13	-17.33	3.81	2.89	0.32
		14	-18.04	5.17	3.84	0.09
		15	-18.92	6.24	3.68	0.02
6	0.05	13	-16.68	1.34	1.36	0.31
		14	-17.23	1.35	2.83	0.38
		15	-18.48	2.88	1.67	0.3
	0.15	13	-17.18	2.46	2.09	0.38
		14	-17.8	3.31	3.55	0.19
		15	-18.92	4.57	2.19	0.07
	0.3	13	-17.49	3.61	2.69	0.32
		14	-18.18	4.93	3.84	0.09
		15	-19.07	6	3.1	0.02
8	0.05	13	-16.88	1.2	1.23	0.22
		14	-17.37	2.54	2.94	0.35
		15	-18.66	2.75	1.57	0.28
	0.15	13	-17.41	2.64	2.03	0.38
		14	-18.08	2.89	2.97	0.2
		15	-19.1	4.13	1.76	0.07
	0.3	13	-17.75	3.16	2.56	0.31
		14	-18.41	4.24	3.67	0.11
		15	-19.26	5.47	3.47	0.03

Note. — Column names are same as Table A.1

Table A.3 IPP properties of the models for SN2020bvc with $f_{\rm m}$= 0.9

$E_{\rm burst}$ [B]	$M_{\rm CSM}$ [$M_\odot$]	log$R_{\rm CSM}$ [cm]	$M_{g,\rm IPP\,peak}$ [mag]	$t_{\rm rise}$ [d]	$\Delta t_{+0.3}$ [d]	$s_{3\sim10\rm d}$ [mag/d]
6	0.05	13	-16.91	1.37	1.20	0.01
		14	-17.38	1.79	2.48	0.06
		15	-18.52	2.81	2.23	0.05
	0.1	13	-17.20	1.94	1.67	0.04
		14	-17.88	2.52	2.28	0.07
		15	-18.88	3.84	1.65	0.06
	0.2	13	-17.49	2.75	2.40	0.06
		14	-18.23	3.85	3.05	0.06
		15	-19.14	5.06	2.34	0.04
9	0.05	13	-17.21	1.14	1.09	0.00
		14	-17.66	1.74	2.31	0.06
		15	-18.83	2.75	2.08	0.07
	0.1	13	-17.54	2.13	1.57	0.04
		14	-18.19	2.32	2.42	0.08
		15	-19.29	3.41	1.30	0.07
	0.2	13	-17.88	2.41	1.9	0.06
		14	-18.57	3.24	2.85	0.07
		15	-19.43	4.42	1.21	0.04
12	0.05	13	-17.39	1.05	1.04	0.02
		14	-17.92	2.14	2.02	0.07
		15	-19.02	2.50	2.20	0.09
	0.1	13	-17.75	1.56	1.43	0.04
		14	-18.38	2.17	2.19	0.08
		15	-19.50	3.24	1.15	0.07
	0.2	13	-18.10	2.48	1.88	0.07
		14	-18.81	3.01	2.64	0.07
		15	-19.65	3.91	1.35	0.05

Note. — Column names are same as Table A.1 except for $M_{g,\rm peak}$: g-band maximum magnitude during the IPP; $t_{\rm rise}$: time from the explosion to the g-band maximum during the IPP, $\Delta t_{+0.3}$: time span between two 76% g-mag maximum (+0.3 mag) points during the IPP, one during its rise to the maximum and the other during its decline from the maximum; $s_{3\sim10\rm d}$: $g-r$ color evolution slope at 3∼10 day.

요 약

초신성 모체성에 관해 항성 진화론적, 관측적, 우주론적 등의 다양한 관점에서의 논의가 진행되어왔다. 소수의 경우를 제외하고는 초신성 폭발 전 모체성의 직접적인 관측이 이루어진 경우가 없지만 우리는 폭발 후의 관측 데이터로부터 그 성질을 유추할 수 있다. 초신성의 광도 곡선과 색지수는 모체성의 화학 조성과 초신성의 역학적인 특성을 규명하는데 중요한 측광학적 성질이다. 본 학위 논문에서는 초신성의 광도 곡선과 색지수를 통해 이전까지는 깊이 논의되지 않았던 Ic형 초신성 모체성의 별주위물질과, Ib형, Ic형 초신성의 색지수 차이를 통해 두 모체성의 차이를 규명해보고자 했다. 연구는 STELLA라는 초신성 폭발 시뮬레이션 프로그램을 사용하여 모델을 만들고, 관측과 모델을 비교하는 방식으로 진행되었다.

첫번째 연구에서는 폭발 직후 충격파로 인해 축적된 열에너지에서 대부분의 에너지가 공급될 때 가시광 영역에서 밝은 빛을 내는 특이한 Ic형 초신성에 주목했다. Ic형 초신성의 모체성은 수소 외곽과 헬륨 외곽을 대부분 잃은 밀집성으로, 충격파가 진행함에 따라 큰 단열 팽창을 겪게 된다. 아직 니켈의 방사성붕괴로 인한 에너지 공급이 광구까지 도달하지 못한 초기에는 가시광 영역에서 밝기가 어두운 것이 일반적인 경우였다. 하지만 이제까지 관측된 Ic형 초신성 중 세 경우(LSQ14efd, iPTF15dtg, SN 2020bvc)는 초기에 밝은 광도 곡선을 보여준다. 이러한 특성은 모체성이 폭발 직전 형성한 별주위물질로 설명할 수 있다. 시뮬레이션을 통해 별주위물질의 질량, 반경, 밀도 구조 등의 변수에 따라 초기 광도 곡선의 밝기, 지속 시간, 색지수 진화 양상 등이 달라짐을 확인하였다. 관측과 모델의 광도 곡선과 색지수 진화 비교를 통해 각 초신성 데이터를 가장 잘 설명하는 모델을 찾았다. 세 초신성의 모체성은 모두 $0.1 M_{\odot}$에 달하는 질량의 별주위물질을 가지고 있던 것으로 예측되었다. 그에 해당하는 질량 손실은 초신성이 폭발하기 1년 전 이후부터 $\dot{M} \gtrsim 1.0\ M_{\odot}\ \mathrm{yr}^{-1}$ 정도로, 이는 기존에 알려진 항성풍이나 분출 현상으로는 설명할 수 없어 이런 극심한 질량 손실을 일으키는 새로운 기작이 필요하다고 생각된다.

두번째 연구에서는 문헌에 있는 Ib형, Ic형 초신성의 측광 데이터를 수집해 V-밴드

에서 최대 밝기를 보일 때 색지수 $B-V$의 분포를 비교해보았다. 그 결과 Ib형이 Ic형에 비해 더 작은 (푸른) 색지수 분포를 보여주었다. 이를 설명하기 위해 세 가지 가능성이 검토되었다. 첫째로 Ib형 초신성과 Ic형 초신성의 모체성의 화학 조성이 다른 경우, 둘째로 니켈의 분포가 다른 경우, 셋째로 니켈의 질량의 분출물의 질량에 대한 비가 다른 경우가 색지수의 차이를 만들 것이라 예측되었다. 헬륨 외곽을 가지고 있는 모체성과 헬륨 외곽을 잃은 모체성을 토대로 다양한 분출물 질량, 니켈 질량, 니켈 분포, 운동 에너지를 가정하여 많은 수의 초신성 모델을 만들었다. 각 변수에 대해 색지수 분포 변화를 조사한 결과, Ib형 초신성의 경우 헬륨 외곽이 남아 있는 모체성, Ic형 초신성의 경우 헬륨 외곽을 잃은 모체성이 관측을 잘 설명함을 확인했다. 결론적으로 Ib형, Ic형 초신성 모체성은 화학 조성과 니켈 분포가 달랐을 것으로 예상된다.

주요어: 초신성: 일반 – 항성: 무거운 별 – 방법: 수치 해석

학 번: 2019-22292